A Bottom-Up Optimization Approach for Friction Stir Welding Parameters of Dissimilar AA2024-T351 and AA7075-T651 Alloys

K.S. Anil Kumar, S.M. Murigendrappa, and Hemantha Kumar

In the present study, optimum friction stir weld parameters such as plunge depth, tool rotation speed and traverse speed for butt weld of dissimilar aluminum alloy plates, typically 2024-T351 and 7075-T651, are investigated using a bottom-up approach. In the approach, optimum FSW parameters are achieved by varying any one parameter for every trial while remaining parameters are kept constant. The specimens are extracted from the friction stir-welded plates for studying the tensile, hardness and microstructure properties. Optimum friction stir weld individual parameters are selected based on the highest ultimate tensile strength of the friction stir-welded butt joint specimens produced by varying in each case one parameter and keeping the other two constant. The microstructure samples were investigated for presence of defects, grain refinement at the weld nugget (WN), bonding between the two materials and interface of WN, TMAZ (thermomechanically affected zone) of both advancing and retreating sides of the dissimilar joints using optical microscopy and scanning electron microscopy analyses. In the experimental investigations, the optimum FSW parameters such as plunge depth, 6.2 mm, rotation speed, 650 rpm and traverse speed of 150 mm/min result in ultimate tensile strength, 435 MPa, yield strength, 290 MPa, weld joint efficiency, 92% and maximum elongation, 13%. The microstructure of optimized sample in the WN region revealed alternate lamellae material flow pattern with better metallurgical properties, defect free and very fine equiaxed grain size of about 3-5 µm.

1. Introduction

Friction stir welding (FSW) is proven as a successful solid-state metal joining technique, and it has a significant role in reducing the difficulties and defects to a much greater extent in the welding process when compared to the conventional joining techniques (Ref 1). Joining of different types of aluminum alloys series by conventional fusion welding technique like tungsten inert gas welding, etc., introduces serious problems like porosity, slag inclusion, solidification cracks, etc., resulting in increasing complexity in manufacturing and cost (Ref 2). During FSW, a non-consumable tool with typical pin profile traversed along the weld line to obtain joints of sheets or plates. The optimization of FSW parameters results in an enhancement in mechanical properties of the similar or dissimilar joints, free of defects such as wormhole, pin hole, tunnel, piping, hooking, etc. Among all the FSW parameters (Ref 2, 3), the most influencing parameters are tool rotation speed, welding speed and tool pin profile. These FSW parameters play a vital role in

overall improvement in the mechanical properties of the FSW joints.

Most of the optimization procedures reported in literature (Ref 4-8), the optimum FSW parameters were achieved by computational techniques, analytical methods, numerical methods and experiments. The design of experiments (DOE), such as Taguchi, response surface method (RSM) and artificial neural network (ANN), has been used to optimize the FSW parameters. Shojaeefard et al. (Ref 4) report cellular automaton (CA) method to simulate the grain structure of the weld zone and conducted experimental trials to find the optimum combination of FSW parameters using Taguchi technique. Okuyucu et al. (Ref 5) and Shojaeefard et al. (Ref 6) developed an artificial neural network (ANN) model to analyze the experimental data and predict the correlation between FSW parameters and mechanical properties and thus obtained the optimal combinations of FSW parameters. Salehi et al. (Ref 7) and Javadi et al. (Ref 8) optimized the FSW process parameters using Taguchi technique. Rajakumar et al. (Ref 9) developed the relationship between input FSW parameters such as axial force, tool pin, shoulder diameter, rotation speed and welding speed. Further, they studied its effect on output responses on tensile strength, hardness and corrosion rate in joining similar aluminum alloy of typical AA1100 using RSM and obtained optimum FSW parameters. Balasubramanian (Ref 10) studied the influence of the FSW parameters such as rotation speed and welding speed on similar FSW butt joint properties of different aluminum alloys (AA1050, AA6061, AA2024, AA7039, AA7075) and established empirical relationship between FSW parameters and base metal properties to predict the FSW parameters in order to fabricate defect-free joints. All these reported in literatures involve a complex relationship

K.S. Anil Kumar, S.M. Murigendrappa, and Hemantha Kumar, Department of Mechanical Engineering, National Institute of Technology Karnataka, Surathkal 575025, India. Contact e-mail: anilkumar_aks@rediffmail.com.

between input and output parameters. In addition, it is difficult to attain similar conditions in the FSW experiments as predicted in numerical techniques and simulations. Nadammal et al. (Ref 11) have developed a bottom-up approach to optimize the few major friction stir processing parameters like vertical pressure on the tool (plunge depth), tool rotation speed and tool traverse speed to improve the mechanical properties of 2024-T3 aluminum alloy.

The aluminum alloys of typical 2000 and 7000 series due to their high strength-to-weight ratio are widely used in aerospace, marine industries and in structural applications. Many literatures (Ref 12-14) report some studies on FSW of dissimilar AA2024-T3 and AA7075-T6. Cavaliere et al. (Ref 12) studied the mechanical properties of dissimilar FSW joints of AA2024-T3 and AA7075-T6 aluminum alloy by tensile and fatigue tests. These investigators reported experimental work for a constant welding speed of 2.67 mm/s, however, they have not provided sufficient information on the rotation speed. In identifying appropriate FSW parameters, Da Silva et al. (Ref 13) studied the effect of tool rotation speeds (400, 1000 and 2000 rpm) and axial forces (13.4, 12 and 9.8 kN) on material flow and mechanical behavior of FSW joints of typical AA2024-T3 and AA7075-T6 alloy. They recommend tool rotation speed of 1000 rpm and welding speed of 254 mm/min based on the joint weld efficiency of 96%.

Several literature (Ref 14-19) reported that the quality and properties of the two dissimilar FSW joint are affected by material location, FSW process parameters such as tool rotation speed and welding speed, material flow between advancing side (AS) and retreating side (RS). Also the weld zone of the dissimilar joints exhibits three different kinds of region, namely unmixed region (UMR), mixed flow region and mechanically mixed region (MMR). The UMR consists of microstructure of any one type of material. The mixed flow region is characterized by alternate layer-by-layer forming of a lamellae pattern consisting of both the material, and the MMR contains the microstructure of both the materials. Khodir et al. (Ref 14) examined the effect of different welding speed of 0.7, 1.2, 1.7, 3.3 mm/s with a constant tool rotation speed of 1200 rpm on microstructure and mechanical properties of AA2024-T3 and AA7075-T6 joints. They report the presence of onion ring patterns in the stir zone and concluded that locating AA2024-T3 on the AS results in highest joint efficiency in terms of tensile strength of 423 MPa with welding speed of 1.67 mm/s. Guo et al. (Ref 15) studied the effect of material location and traverse speed on the material flow, microstructure and mechanical properties of the dissimilar joints between AA6061 and AA7075. They further report the material mixing in nugget zone was much more effective when low-strength AA6061 was located on the AS. They also report that locating AA6061 in the AS results in highest joint strength of 245 MPa at traverse speed of 5 mm/s and constant rotation speed of 1200 rpm. A similar observation was reported by Park et al. (Ref 16) in their investigation carried out to find the effect of material location in a dissimilar FSW joint of AA5052-H32 to AA6061-T6 using constant rotation speed 2000 rpm and traverse speed of 100 mm/min. These authors found that the materials more properly mixed when low-strength AA5052-H32 was placed in the AS and AA6061-T6 in the RS. Rodriguez et al. (Ref 17) studied the effect of tool rotation speed on joint strength of dissimilar butt joints of AA6061-to AA7050 by placing AA7050 in the AS and found that increase in the tool rotation speed increased the strength and material

mixing. They also reported a decreasing trend in the mechanical strength and failure of the joints at stir zone due to inadequate material intermixing at low tool rotation speed. Dinaharan et al. (Ref 18) studied the contribution of material placed in AS and RS at four rotation speeds (800, 1000, 1200 and 1400 rpm) on cast and wrought aluminum typical AA6061 alloy. The authors observed that for the tool rotation speeds 800 and 1000 rpm, the material kept at RS occupies a major portion of the weld zone. However, for increased tool rotation speeds from 1200 rpm to 1400 rpm, more contributions of the material kept at AS result. They also observed that as increasing rotation speed results in higher tensile strength irrespective of the material location. Ouyang and Kovacevic (Ref 19) studied the material flow and microstructure of dissimilar alloys between AA6061 and AA2024 and report that the nugget zone of AA6061 and AA2024 alloy consists of MMR, UMR and stirring-induced plastic flow region (SPFR). They further report that increasing the rotation speed results in improvement in mechanical mixing of the dissimilar welds at the nugget zone.

Few researchers in their investigations (Ref 20-22) also examined the effect of tool pin geometries, tool shoulder contact and axial force (i.e., plunge depth) on the material flow and tensile strength of the weld joint. Kumar and Kailas (Ref 20) conducted the experiments to study the effect of the tool shoulder on material flow on similar joints of AA7020 and found that that proper interaction of the tool pin and shoulder will result in better material flow and produce defect free joints. They further report that an axial force of 8.1kN produces defect-free weld joint. Sundaram and Murugan (Ref 21) in their investigation on dissimilar joints of AA2024-T6 and AA5083-H321 report that both lower axial force of 15kN and higher axial force of 35kN result in decrease in the tensile strengths. Buffa et al. (Ref 22) investigated the effect of different pin geometries, pin angle and welding speed on the FSW process with a numerical model and found that an optimal combination of welding speed of 100 mm/min and pin angle of 40° result in good joint strength. They also found that sufficient amount of frictional heat results in a defect-free weld joints. Vijayavel et al. (Ref 23) investigated the effect shoulder diameter-to-pin diameter ratio on tensile strength, hardness and microstructure of LM25AA-5% SiCp metal matrix composites and found that higher heat generation results in lower tensile, hardness and wider processed weld zone. Rajakumar et al. (Ref 24) in their study on 7075-T6 joint found that the effect of rotational speed of 1400 rpm, welding speed of 60 mm/min, axial force of 8kN, shoulder diameter of 15 mm and pin diameter of 5 mm results in higher joint strength. The effect of the tool rotational speed and pin profile on mixed flow and unmixed flow region at the weld zone region of dissimilar weld joint of AA5083-H111 to AA6351-T6 was reported by Palanivel et al. (Ref 25). These researchers investigated the importance of different rotational speed in obtaining mixed flow region and therefore its effect on tensile strength of the joints. Amancio et al. (Ref 26) in their study also report the weld zone of dissimilar FSW joints consisting of alternate lamellae pattern of both AA2024-T351 and AA6056-T4. In the investigation conducted by Steuwer et al. (Ref 27), the rotational speed found to have greater influence on residual stress distribution than the traverse speed on dissimilar joints of AA5083 and AA6082. Peel et al. (Ref 28) investigated the effect of traverse speed on mechanical properties, heat input and residual stresses of the AA5083 joints. They also found that size of the weld zone is influenced by traverse speed and heat input. Zhang et al. (Ref 29) in their

study found that at constant traverse speed, increase in tool rotation speed from 350 to 950 rpm results in drastic decrease in tensile strength of the weld joint.

Most of the FSW literature (Ref 4-10) report the optimization of FSW parameters involves the procedure complexity and more numbers of experimental runs leads to difficulty in building some of the key relations between input and output parameters. An experimental technique-associated bottom-up approach for obtaining the optimum FSW parameters is one of the potential candidatures to eliminate complexity in the procedure further with few numbers of runs. Also, to the authors' knowledge, the optimization of FSW parameters for dissimilar joints by bottom-up approach was not found to be followed in the literatures reported. The present study focuses on the selection of optimum FSW parameters using a bottom-up approach for dissimilar welded aluminum alloys. In this study, the three parameters such as tool plunge depth, tool rotation speed and tool traverse speed are optimized. The dissimilar joints were obtained using high strength aluminum alloys AA2024-T351 and AA7075-T651. The cylindrical taper threaded tool with constant tilt angle 2° has been considered for all experimentations. The mechanical properties, microstructure and fractography analyses of fabricated FSW joints have been evaluated.

2. Experimental Technique for Bottom-Up Approach

A bottom-up approach (Ref 11) has been used to investigate the influence of tool parameters such as plunge depth, rotation speed and traverse speed in friction stir welding. The approach is typically an optimization technique involving two important aspects. In the first case, each experimental trial focuses on the effect of the major individual parameter (plunge depth or rotation speed or traverse speed) on the mechanical and metallurgical properties of the FSW dissimilar joint, rather than all the three major FSW parameters. A bottom-up approach assumes that each individual parameter shows the improvement in joint properties of the dissimilar weld. In the approach, optimum individual parameters are achieved by varying any one parameter for every trial, while remaining parameters are kept constant. Whereas in the second case, the range of parameters that can be investigated using a bottom-up approach in single experimental trial is much larger in numbers when compared to the other DOE techniques (e.g., Taguchi, RSM, etc.) and requires more number of experimental runs and trials. Figure 1 depicts the bottom-up approach procedure.
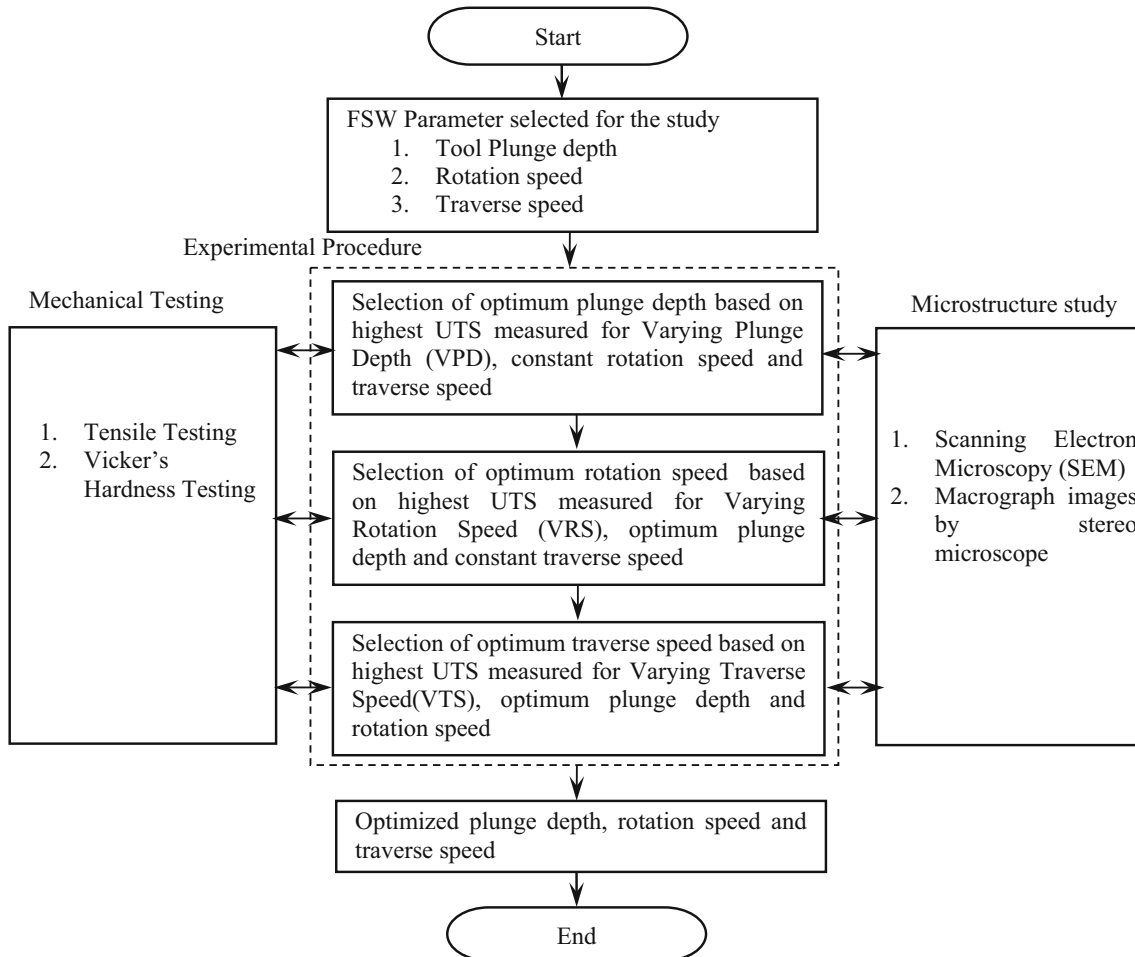

Fig. 1 Flowchart of bottom-up approach

Table 1 Chemical composition of 2024-T351 and 7075-T651 aluminum alloys

Material type	Cu	Mg	Cr	Zn	Mn	Si	Fe	Ti	Al
2024-T351	4.38	1.5	0.01	0.02	0.49	0.05	0.12	0.05	Balance
7075-T651	1.3	2.3	0.19	5.6	0.02	0.03	0.14	0.05	Balance

**Table 2 Mechanical properties of 2024-T351 and 7075-T651 aluminum alloys**

Material type	Yield strength, MPa	Ultimate tensile strength, MPa	Elongation,%	Vickers microhardness at 1kgf load at 15 s, Hv
2024-T351	406	477	17	138
7075-T651	529	564	13	160

2.1 Materials and Machine

The experiment was carried out for joining two rolled alloy metal plates, typically AA2024-T351 and AA7075-T651, having 6.35 mm thickness. All the plates were considered for the tests with dimensions of 200 mm long and 100 mm wide (along rolling direction). The nominal chemical compositions in weight percentage and tensile properties of these two grade alloy plates are given in Tables 1 and 2, respectively. A taper threaded cylindrical tool as shown in Fig. 2 made from hot die steel material and in H13 hardened condition was used for joining two plates. The tool geometry that consists of shoulder diameter, d = 20 mm, which was chamfered from a cylinder diameter, D = 25 mm, height of cylinder, H = 25 mm, pin bottom diameter, d_1 = 6 mm, pin top diameter, d_2 = 7.5 mm, thread pitch equal to 1.5 mm and pin probe length, L = 5.8 mm, has been used for fabricating the joints. A five-axis FSW machine (Make BISS, Model type SP-02-05-05) capable of varying the tool plunge depths, rotation speeds and traverse speeds during the welding process was used for fabrications of the joints. Figure 3 illustrates the arrangement of clamped dissimilar plates within the mounting area of the FSW machine. Figure 4 presents a square butt edge joint of two dissimilar plates produced by FSW line perpendicular to the rolling direction, such that the tool pass was in the y-direction. The orientations of both rolled plates were ensured in the x-direction. The location of AA2024-T351 was always advancing side (AS), and the single pass welding was carried out for all the experiments considered in this study.

2.2 Optimization Experiment Procedures by Bottom-Up Approach

In the bottom-up approach, optimization of FSW parameters such as tool plunge depth in the workpiece, tool rotation speed and tool traverse speed are achieved by varying one parameter at a time while other two parameters were kept constant. Optimization of each parameter is carried out in three different sets of experiment and on individual plates. Figure 5 also presents the orientation of the specimen extraction for studying the tensile and microstructure properties. The order of optimizations performed for the FSW parameters is (1) tool plunge depths, (2) tool rotation speeds and (3) tool traverse speeds. The optimization procedure by bottom-up approach for each of the above cases of FSW parameters is discussed in the following sections.
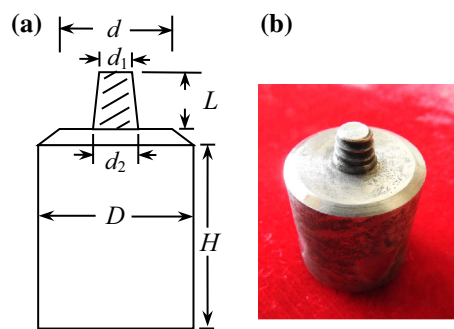

Fig. 2 (a) Schematic of taper threaded cylindrical tool used for FSW of dissimilar joints and (b) photograph of tool
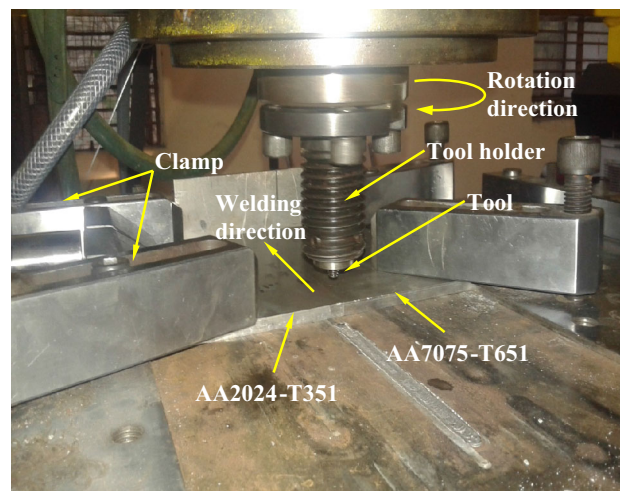

Fig. 3 Photograph of arrangement of clamped dissimilar plates with tool

2.2.1 Optimization of Tool Plunge Depth by Varying Plunge Depth. The experiment trails for varying plunge depth (VPD) were carried out by varying the plunge depth in the range from 5.8 to 6.2 mm along the y-direction for the weld length of 150 mm. Tool rotation speed and traverse speed, 1000 rpm and 120 mm/min, respectively, were kept as constants. Initially, the 5.8 mm length of the tool pin was plunged to a depth of 5.8 mm into the base materials exactly at the weld line of the butt joint, and then, FSW was achieved by linearly
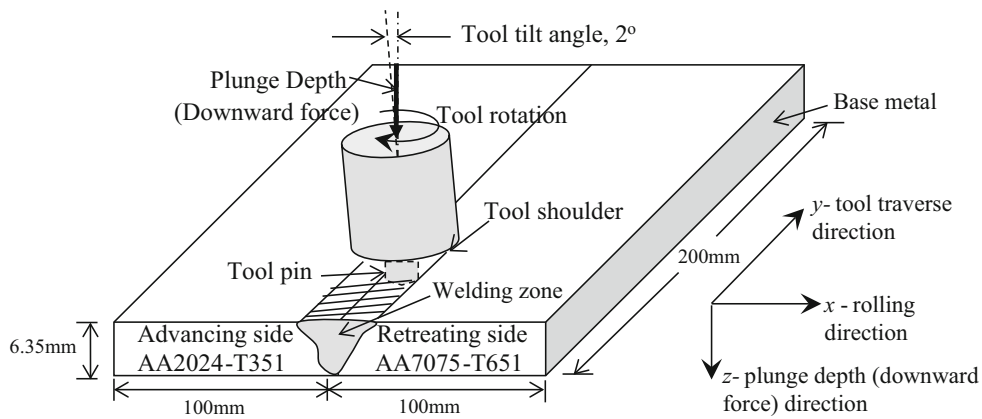
Fig. 4 Schematic of a square butt edge joint
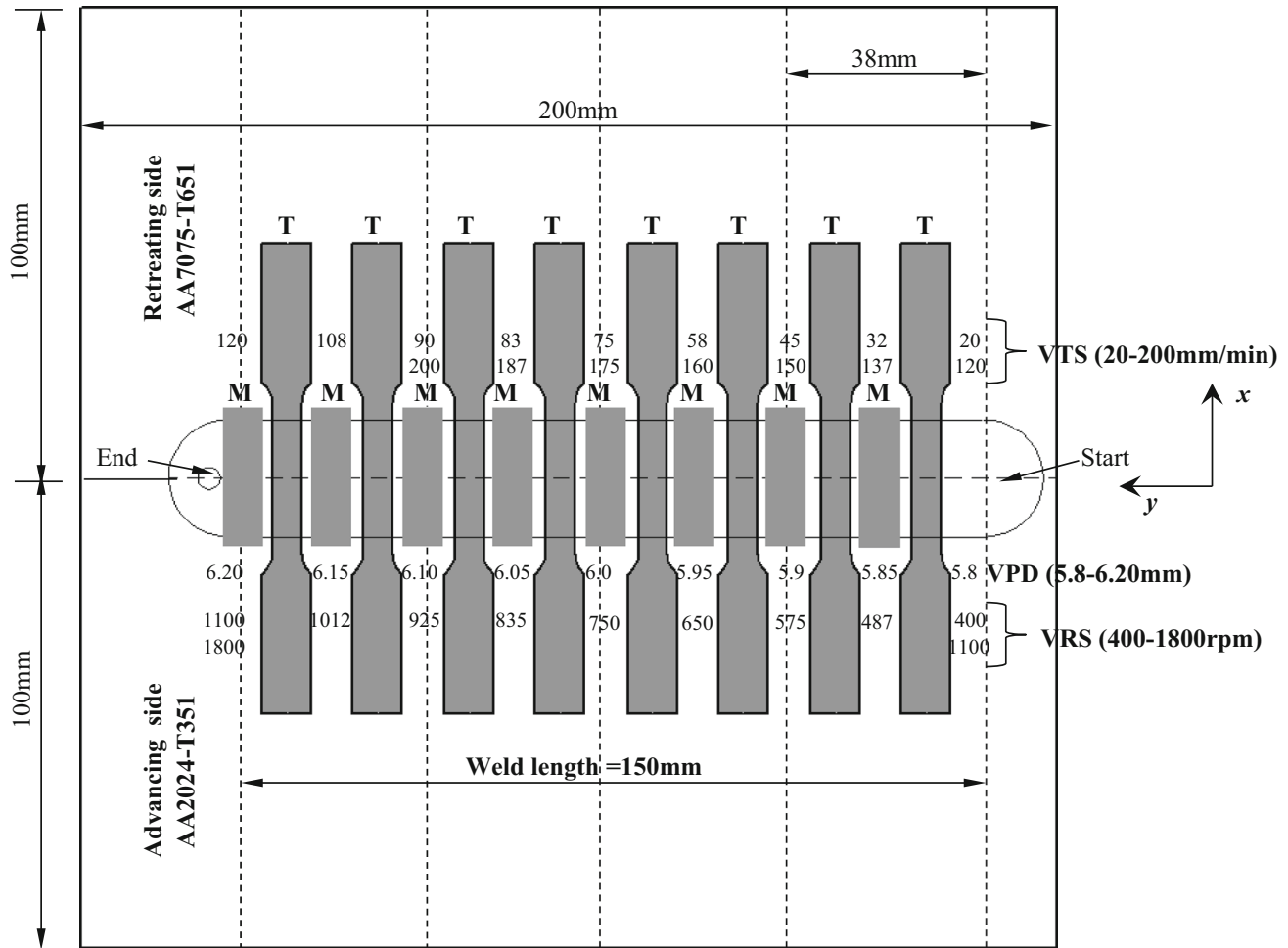
Fig. 5 Schematic of square butt joint of two dissimilar plates: T-orientation of tensile specimens for extraction and M-zone of microstructural samples

increasing the depth till it reaches 6.2 mm at the end of the weld. Figure 6 depicts the FSW of VPD experiment. In the beginning of the FSW process, the plunge depth was selected as 5.8 mm because at this depth the shoulder of the tool makes a contact with the faying surface of the dissimilar plates to be welded. The maximum tool plunge depth of 6.2 mm was selected in order to avoid any possible damage to the tool pin when it makes contact with the surface of the plate mounting area of the FSW machine at higher plunge depth. Microstructure samples (M-zone in Fig. 5) extracted from the FSW joint were investigated for the presence of defects, bonding between the two materials and grain refinement at the WN, AS and RS
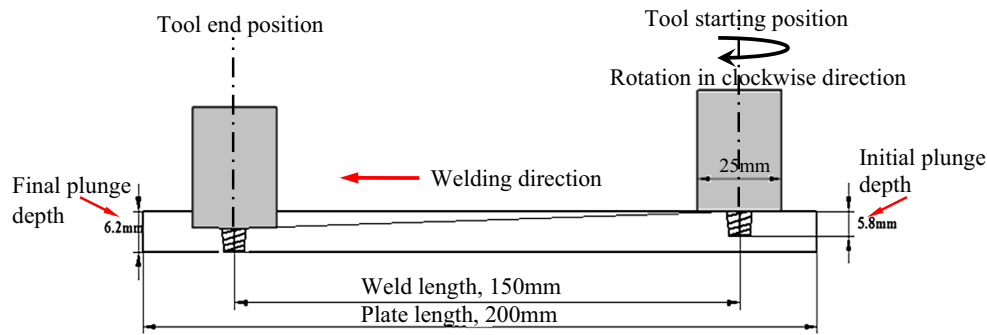
Fig. 6 Schematic of the tool pass in linearly varying plunge depth from 5.8 to 6.2 mm in the *z*-direction for weld length of 150 mm

of the dissimilar joints using optical microstructure and SEM analyses. The optimum tool plunge depth was selected for the specimen considered in the study based on highest UTS.

2.2.2 Optimization of Tool Rotation Speed by Varying Rotation Speed. In varying rotation speed (VRS) experiments, the tool rotation speed varied from 400 to 1800 rpm, by keeping both optimum plunge depth, obtained from the preceding VPD experiment and traverse speed of 120 mm/min as constant. The VRS experiment was carried out in two sets of experiment trails and on an individual set of plate for the same weld length of 150 mm. In the first set of experiment trail, the rotation speed varied from 400 to 1100 rpm and in the second set of experiment trail, the tool rotation varied from 1100 to 1800 rpm. Samples were extracted by adopting the similar way as demonstrated in the preceding section for tensile testing and microstructure study for all set of VRS experiment. Optimum rotation speed was selected based on the highest UTS obtained for the tensile specimen tested at different rotational speeds considered here. The microhardness distribution, optical macrograph and SEM details were obtained for each microstructure sample.

2.2.3 Optimization of Tool Traverse Speed by Varying Traverse Speed. In varying traverse speed (VTS) experiment case, only traverse speed was varied from 20 to 200 mm/min and optimum plunge depth and rotation speed obtained from the preceding sections of VPD and VRS experiments were kept as constant. In this case also, the experiment was carried out in two steps. In the first set, the experiment was carried out by varying the traverse speeds from 20 to 120 mm/min and in the second set, the traverse speed varied from 120 to 200 mm/min. Samples were extracted by adopting the procedure described in preceding sections for tensile testing and microstructure study for all set of VTS experiment. Optimum traverse speed was selected based on the highest UTS. The microhardness distribution, optical macrograph and SEM images were obtained for each microstructure sample.

2.3 Mechanical Testing

In the present study, the mechanical properties such as ultimate tensile strength, yield strength (YS) and hardness have been measured for FSW specimens.

2.3.1 Tensile Properties Testing. The tensile specimens were extracted from the dissimilar FSW joints as depicted in Fig. 5 fabricated for VPD of 5.8-6.2 mm, VRS of 400-1800 rpm and VTS of 20-200 mm/min. For test, servo hydraulic tensile testing machine (Make SHIMADZU and type AGS-X series) of a capacity 100kN at a strain rate of 0.001 s^{-1}

was used. The specimens were prepared according to the American Society for Testing of Materials of code E8 M-04 and were machined perpendicular to the *y*-direction using wire cut electrical discharge machining process. The load and displacement data were recorded. From the recorded load–displacement data, the plots of stress–strain were obtained for the evaluation of UTS, YS and percentage elongation of the FSW samples.

2.3.2 Microhardness Testing. Microhardness testing was carried out on the specimens extracted for microstructure analyses. The tests were performed only for the FSW specimens fabricated for VRS and VTS conditions. The hardness of the specimens was measured using a micro-Vickers hardness testing machine (make SHIMADZU, type HMV-G20-S7) applying a load of 1kgf for 15-s holding time. The location of the indent was selected with a depth of 3 mm from the *xy*-plane and across the transverse section of the specimen produced by FSW dissimilar joint. Further, few distinct zones of a FSW specimen such as weld nugget zone (WN), thermomechanically affected zone (TMAZ), heat-affected zone (HAZ) and base material adjoining the HAZ of both AS and RS of the joints zone were considered for hardness measurement.

2.4 Macro- and Microstructure Examinations

The microstructure specimens extracted (indicated as M in Fig. 5) from the dissimilar FSW joints for the condition performed at VPD, VRS and VTS experiments have been carefully prepared according to the standard metallographic procedure to study the macro- and microstructures features. For metallographic examination, three stages of surface polishing were performed. In the first stage, samples were polished using SiC papers with grades from P400 to P3000. In the second stage, specimens were polished using alumina powder with particles of size 1 micron on the disk-type polishing machine. In the last case, fine polishing of surface was achieved using diamond particles of 0.5 microns. The samples were etched with standard Keller's reagent prepared using 1 ml of HF, 2.5 ml of HNO$_3$, 1.5 ml of HCl and 95 ml of distilled water. The macrostructure examination was performed by covering the areas of the WN, the interface between WN and TMAZ of both AS and RS of the fabricated joints for the investigation of joint quality using a stereo zoom microscope with low magnification of $10 \times$ and light optical microscope (AXIO CAM 105). The detail microstructure examination was carried out for three zones followed by WN, TMAZ and HAZ of both AS and RS of the joints using the SEM (make JEOL type JSM-6380 LA). The fractured surface of specimen having the
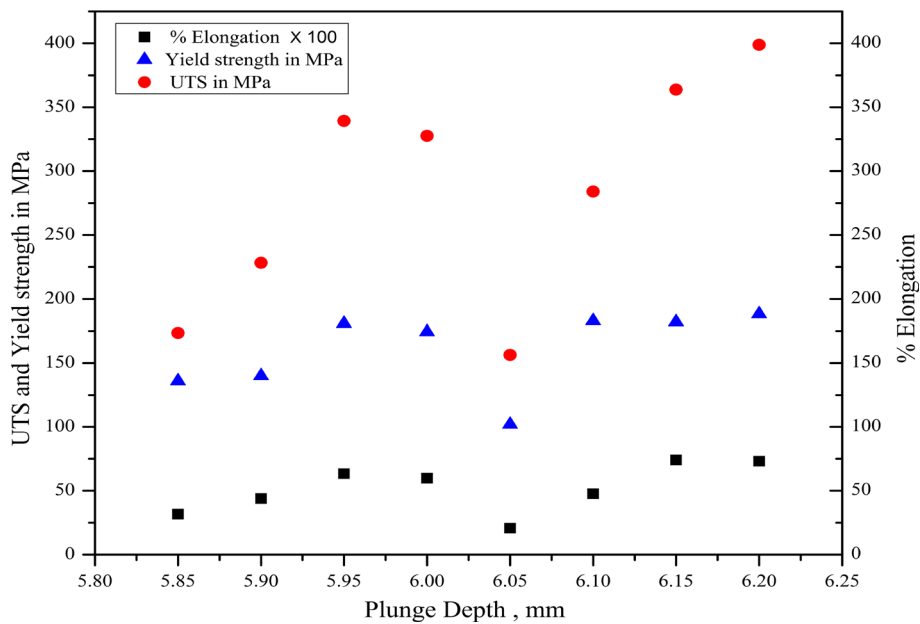
Fig. 7 Variation of UTS, yield strength and % elongation for the case of VPD with 5.8 to 6.2 mm. Note, % elongation is scaled to 100

highest UTS for optimum combination of FSW parameters was observed using SEM.

3. Results and Discussion

3.1 Tensile Properties

The UTS and YS of the FSW specimens tested for varying the plunge depths of 5.8 to 6.2 mm, rotation speeds of 400 to 1800 rpm and traverse speeds of 20 to 200 mm/min are discussed in the following sections.

3.1.1 Varying Plunge Depth Experiment. The results of specimens tested for UTS, YS and percentage elongation for VPD range from 5.8 to 6.2 mm are as shown in Fig. 7. Referring to Fig. 7, it is observed that the UTS, YS and percentage elongation followed the same tendency of variations in their values. Further, lower UTS, YS and the ductility were observed for varying the plunge depth between the ranges 5.8 to 6.05 mm. The UTS of 173 MPa and YS of 136 MPa were observed for the tool plunge depth of 5.8 mm. As expected, this is due to the low plunge depth and lack of good interaction between the shoulder and the base material (Ref 20, 21). During the initial stage of the plunge depth, the primary source of the heat generated was due to the friction between tool shoulder and pin with the workpiece (Ref 2). Improper softening and poor flow of the material observed in the case of lower plunge depth due to low friction between shoulder and workpiece cause insufficient heat generation at local weld zone and result in the formation of defects in the different regions. The possible presence of defects was observed, particularly near the top surface above the WN region. One can observe from the plot that at the beginning the UTS increased from 173 to 327 MPa for the tool plunge depth ranging between 5.8 to 6.0 mm and again UTS decreased to 156 MPa for a plunge depth of 6.05 mm. An increase in the YS from 136 to 180 MPa was also observed for a plunge depth ranging between 5.8 to 6.0 mm
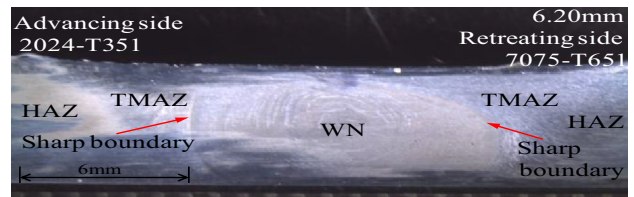
Fig. 8 Macrograph of FSW specimen, free of defects at weld region for the plunge depth of 6.2 mm. Arrow heads pointing to existence of sharp boundaries between the interface of WN and TMAZ

and YS decreased to 101 MPa for a plunge depth of 6.05 mm. As the plunge depth increased above 6.10 mm by increasing the axial load on the pin, sufficient amount of contact between shoulder and pin with the base materials ensured and resulted in sufficient amount of frictional heat generation to facilitate the flow of material and thus increase in UTS, YS and ductility of the weld joint (Ref 20-22, 37). The maximum UTS of 398 MPa, YS of 190 MPa and percentage elongation of 7.31 at a plunge depth of 6.2 mm were also observed from the plot. This depth is considered as an optimum for the case of constant tool rotation speed of 1000 rpm and traverse speed of 120 mm/min.

Figure 8 depicts the macrograph of the transverse section of the FSW specimen obtained for optimum condition of plunge depth with the weld region is free from defects. However, the presence of a sharp boundary between the interface of WN and TMAZ of both AS and RS can be observed. The interface between the WN and TMAZ diffused in the RS, and it is relatively sharp on the AS. These sharp boundary acts as a region of discontinuity, and fracture can occur along any one of these sharp boundaries leading to the early failure of the joints. Figure 9 presents the photograph of the surface morphology of the FSW specimen. The weld crown had smooth surface finish without any defects such as cracks, tunnel and excessive flash for the tool plunge depth between 5.8 to 6.05 mm. However,

the appearance of the surface finish was slightly deteriorated with moderate flash as seen at the weld crown area for the plunge depth range between 6.10 to 6.20 mm.

3.1.2 Varying Rotation Speed Experiment. The effect of varying tool rotation speeds ranging from 400 to 1800 rpm for the optimized plunge depth of 6.2 mm and constant traverse speed at 120 mm/min is as shown in Fig. 10. Figure 10 shows higher UTS, YS and percentage elongation obtained at the tool rotation speed ranging between 500 to 650 rpm. The UTS, YS and percentage elongation are ranging between 417-419 MPa, 185-200 MPa and 11-13%, respectively. The UTS and YS of the dissimilar FSW joint increased from 309 to 419 MPa and from 160 to 200 MPa, respectively, for varying the tool rotation speed from 400 to 650 rpm, respectively. A considerable decrease in the UTS, YS and percentage elongation of the FSW joint was observed as the tool rotation speed increases above 1000 rpm. For the rotation speed above 1250 rpm, the UTS, YS and percentage elongation become sensitive and decreased due to formation of wormhole defects at the FSW joints. Among these varying rotation speeds ranging 400-1800 rpm, the maximum UTS of 419 MPa, YS of 200 MPa and

percentage elongation of 13 achieved for tool rotation speed of 650 rpm. Thus, based on the FSW conditions considered in this, the tool rotation speed of 650 rpm selected as an optimum.

Figure 11 shows the macrograph corresponding to the optimum rotation speed of 650 rpm identified with WN, TMAZ and HAZ regions in the FSW joint. The sharp boundaries between the interface of WN and TMAZ of both AS and RS more diffused when compared to the macrograph of the optimized sample as presented in Fig. 8 from VPD experiment. The surface morphology observed is as shown in Fig. 12. The weld crown shows smooth surface finish as observed in Fig. 12(a). The weld crown surface area observes a smooth and defect-free surface finish for tool rotation speeds ranging between 400 and 700 rpm. However, the deterioration in surface smoothness with excessive flash (Fig. 12a and b) is observed in the weld crown area for above 950 rpm rotation speed, causing thinning in cross section of the welded plates. Better appearance of the weld surface finish with reduced flash and good mechanical performance was observed at lower tool rotation speed ranging between 500 and 650 rpm.

3.1.3 Varying Traverse Speed Experiment. The UTS, YS and percentage elongation obtained for tensile specimen for VTS ranging 20-200 mm/min with optimum plunge depth of 6.2 mm and rotation speed of 650 rpm are as shown in Fig. 13.
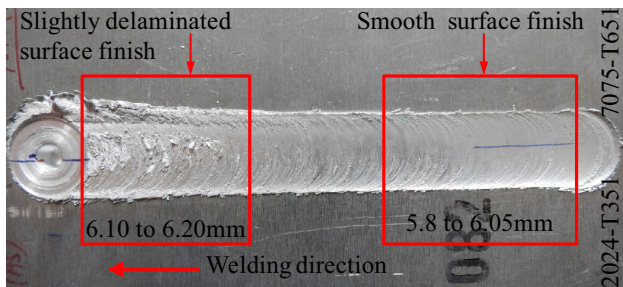
Fig. 9 Surface morphology of FSW specimen plate at welded joint for VPD of ranging from 5.8 to 6.2 mm
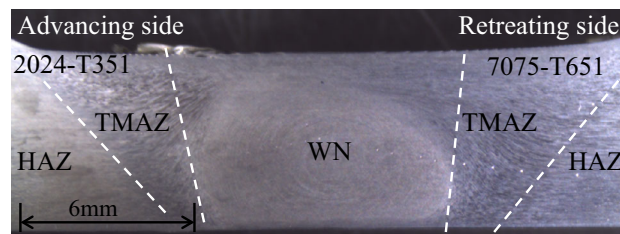
Fig. 11 Macrograph of the FSW specimen for tool rotation speed of 650 rpm, plunge depth of 6.2 mm, traverse speed of 120 mm/min
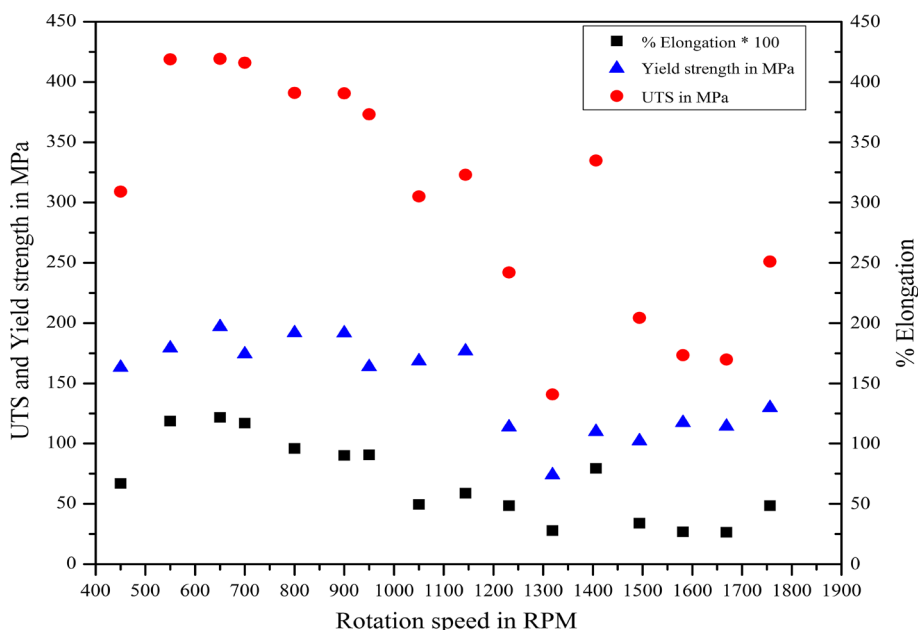
Fig. 10 Variation of UTS, yield strength and % elongation for VRS of 400-1800 rpm. Note, % elongation is scaled to 100
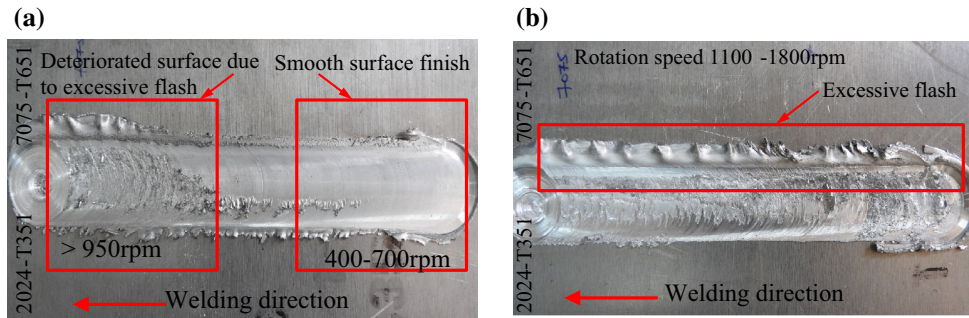
Fig. 12 Photographs of surface morphology of FSW specimen plate for VRS range of (a) 400-1100 rpm and (b) 1100-1800 rpm
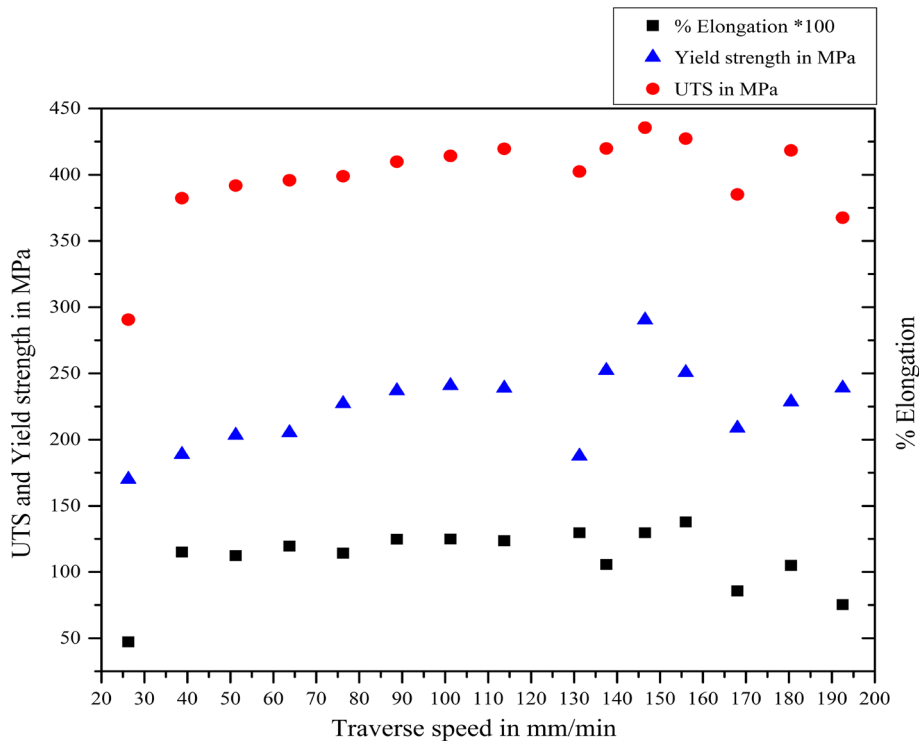
Fig. 13 Variation of UTS and % elongation for VTS range 20-200 mm/min. Note, % elongation is scaled to 100

Lower UTS range between 290 and 390 MPa, YS range between 170 and 200 MPa and percentage elongation observed for a lower traverse speed range from 20 to 50 mm/min. This may be due to increase in frictional heat and slower cooling rate, causing deterioration of tensile properties. Similar observations are reported by investigators (Ref 23, 24). When the tool traverse speed varied from 50 to 80 mm/min, both the UTS and YS found to be almost constant. The UTS, YS and percentage elongation show increase in trend as traverse speed increases ranging from 80 to 150 mm/min. The UTS, YS and percent elongation reached maximum at traverse speed 150 mm/min before falling again for higher traverse speed above 150 mm/min. The change in the tensile properties becomes sensitive above the traverse speed 150 mm/min, and it can be observed from the plot that the UTS, YS and ductility decreased with increasing traverse speed. With increase in traverse speed, low heat input results in lack of metallurgical bonding between two materials (Ref 24) and sharp boundary yields lower strength of the joints. One can conclude from the plot of tensile test results that the joints fabricated at lower traverse speed and higher traverse both have shown lower UTS and YS. The highest value of UTS of 435 MPa, YS of 290 MPa, percentage elongation of 13 and maximum joint efficiency of 92% was obtained for a specimen tested for a traverse speed between 145 and 150 mm/min. Hence, in this range the traverse speed of 150 mm/min selected as an optimum traverse speed. Macrograph of the FSW joint region for a specimen with optimum values of traverse speed, 150 mm/min, plunge depth, 6.2 mm, and rotation speed, 650 rpm, is as shown in Fig. 14. The figure also shows diffused sharp boundaries between interface between WN and TMAZ. The photographs of surface morphology as shown in Fig. 15(a) and (b) consist of smooth surface finish without any defects on weld crown.

3.2 Macro- and Microstructure Observations

All cross-sectional macro- and microstructures observed in the present study for dissimilar FSW joints produced for VPD range of 5.8-6.2 mm, VRS range of 400-1800 rpm and VTS range of 20-200 mm/min are discussed in the proceeding sections.

3.2.1 Varying Plunge Depth Experiment. The optical macrographs and low-magnification SEM images of the transverse cross sections of the dissimilar FSW joint region of the specimens produced for VPD (5.8-6.2 mm) experiments are presented in Table 3 and Fig. 16, respectively. The macrograph (Table 3) for low plunge depth of 5.85 mm shows clear visible pin hole defect above the WN toward the AS. This is also one of the reasons for the decrease in UTS of the joint (Fig. 7). Low plunge depth or lack of shoulder contact with the dissimilar material joint results in less amount of heat input to the material, reduced smoother flow of the material and unmixed region (Ref 13, 20, 21). Similar observation can be seen in the optical macrograph (Table 3) and SEM images (Fig. 16a and b) for the plunge depths 5.85 mm and 5.90 mm, consisting of unmixed region close to the top surface of the weld and thus results in defects above the WN. For the plunge depth of 5.95 mm, the macrograph and SEM image (Fig. 16c) shows no defect at the top of the WN, but there exists a sharp boundary between two materials toward the AS and as well as RS of the joint. These sharp boundaries formed as the result of an insufficient diffusion phenomenon between both the alloys. As observed in macrograph, the plunge depth of 6.0 mm does not show any visible defects, but low-magnification SEM images (Fig. 16d) reveal the presence of crack above the WN and thus result in the decreased UTS (Fig. 7) for the tested tensile specimen. The macrograph (Fig. 16e) for the plunge depth of 6.05 mm shows the interface between WN and TMAZ of RS consisting of a clear visible separation. These discontinuities are weaker region, and fracture can originate along these leading to the early failure of the joints. The lowest UTS

of 156 MPa, YS of 101 MPa (see Fig. 7) can be seen for the plunge depth of 6.05 mm. In the other cases, macrograph and SEM image studies carried out for the plunge depth above 6.10 mm (Fig. 16f), 6.15 mm (Fig. 16g) and 6.20 mm (Fig. 16h) reveal that with the increase in the plunge depth, defects have disappeared (Ref 37). However, a minimum sharp boundary was observed between WN and TMAZ interface on AS and RS. When compared to plunge depth of 6.15 mm, the UTS, YS and percentage elongation (Fig. 7) recorded high for the plunge depth of 6.2 mm and this depth was selected as optimum plunge depth for FSW joint of dissimilar alloys. For this plunge depth, SEM image (Fig. 16i) shows the WN consisting of equiaxed grain structure with an average grain size of 4.5-8 μm.

3.2.2 Varying Rotation Speed Experiment. Specimens produced for the FSW joint conditions of VRS (400-1800 rpm), optimum plunge depth, 6.2 mm, and constant traverse speed, 120 mm/min, were observed using optical stereo microscope and SEM. Table 4 presents optical macrograph of the transverse section of microstructure specimens extracted from dissimilar FSW joints produced for the tool rotation speed range 400-1800 rpm. From the macrograph, it is evident that for the rotation speed range between 400 and 1250 rpm, sound joints are produced without any defects like wormholes, kissing bond or pin hole.

Experiments performed at higher rotation speed above 1250 rpm produced defects in the weld, particularly above the WN and near to the top surface of the weld. Figure 17(a)-(h) shows the low-magnification SEM images for the higher tool rotation speed from 1250 to 1725 rpm. It can be observed from the images (Fig. 17b and h) that joints produced at the higher tool rotation speed of 1250 rpm onwards consists of wormhole defects above the WN and toward the AS. This is due to the excessive plastic deformation and stirring at higher rotation rate, resulting in defects in the weld region (Ref 30). It is also evident from Fig. 10 that at higher rotation speed the tested tensile specimen shows decrease in UTS owing to the presence of a defective weld region. This is consistent with the early investigation reported by Zhang et al. (Ref 29). These authors found that the defects and grain size at WN increased with increasing in rotation speed resulting in decreased tensile strength. In some of the investigations reported (Ref 17), the general observation as tool rotation speed increases the heat input increases. This results in a better material flow, yielding high mechanical strength in the compromise of reduced surface integrity. In the present study also, rotation speed range 400-700 rpm was good enough to produce defect free joints. The observed macrograph (Fig. 11) of the specimen for rotation speed of 650 rpm, optimum plunge depth, 6.2 mm, and
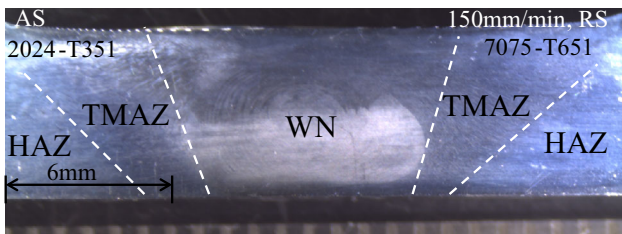

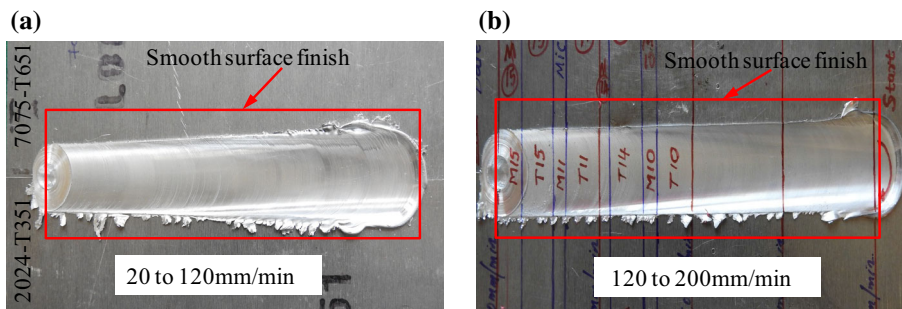**Fig. 14** Macrograph of the FSW specimen for the traverse speed, 150 mm/min

Fig. 15 Photographs of surface morphology of FSW specimen plate for VTS range of (a) 20-120 mm/min and (b) 120-200 mm/min

Table 3 FSW condition and macrographs of dissimilar joints for varying plunge depth experiment. Unit of tool plunge depth in 'mm' indicated on the top right corner of each figure

Tool rotation speed, rpm	Tool traverse speed, mm/min	Varying tool plunge depth, mm	Macrograph	
			Advancing side (AS)	Retreating side (RS)
1000	120	5.85		
1000	120	5.90		
1000	120	5.95		
1000	120	6.00		
1000	120	6.05		
1000	120	6.10		
1000	120	6.15		
1000	120	6.20		

constant traverse speed, 120 mm/min, led to completely defects-free FSW joints. The tested tensile specimen for the 650 rpm resulted in highest UTS, YS and percent elongation (Fig. 10) explained in the previous section of VRS experiment.

3.2.3 Varying Traverse Speed Experiment. Table 5 shows the macrograph of the transverse section of the weld region for the FSW joint specimens produced for the parameter conditions of VTS (20-200 mm/min), optimized plunge depth, 6.2 mm, and optimized rotation speed, 650 rpm. From the macrograph, the influence of traverse speed on the width of WN, TMAZ and HAZ of the weld region can be observed clearly. At the lower traverse speed of 25 mm/min, a flat and wider WN measuring about 11 mm was observed as a result of high heat input (Ref 28) and
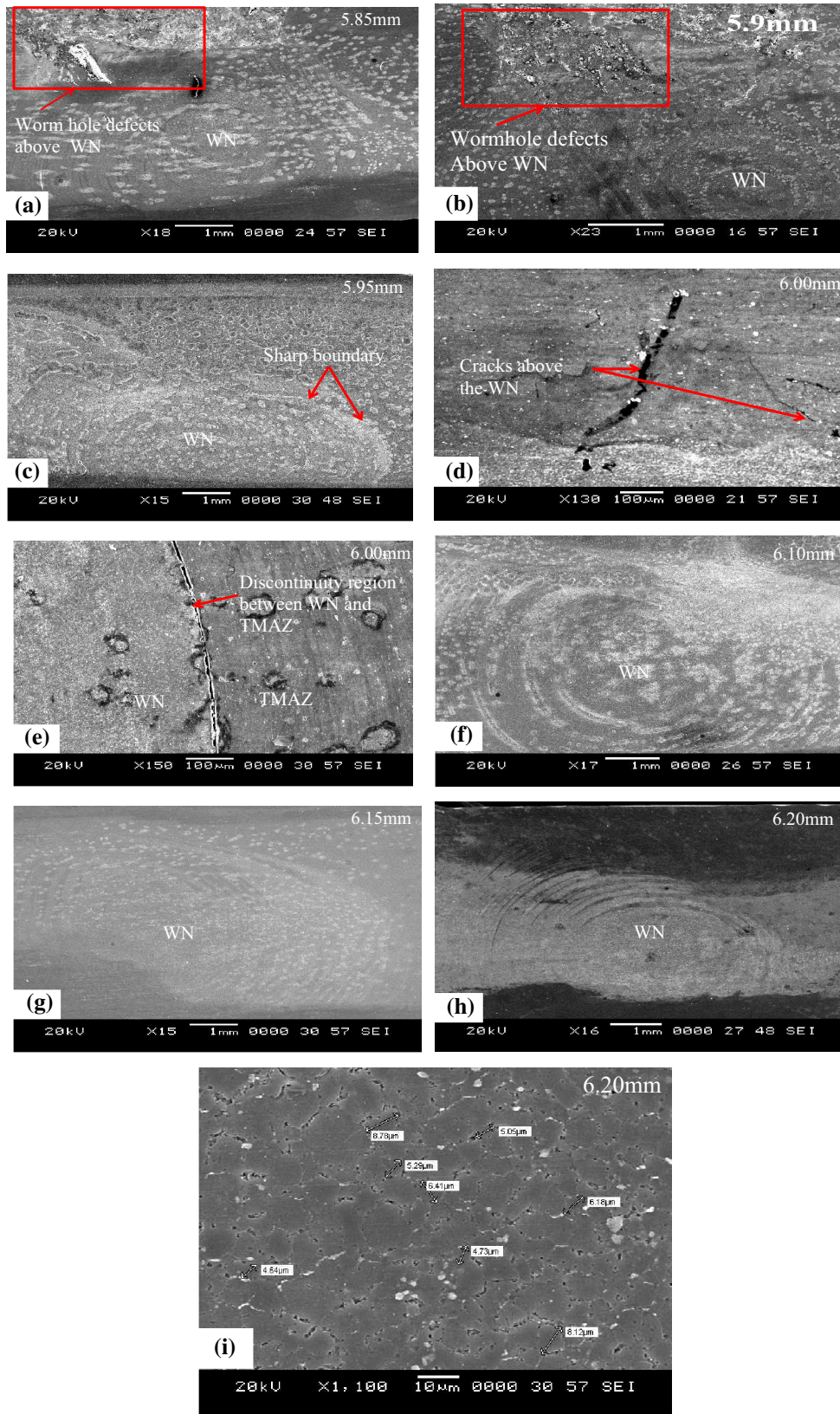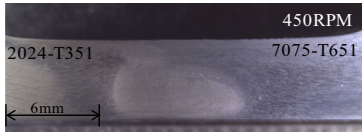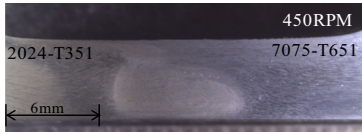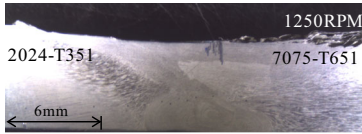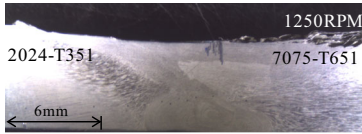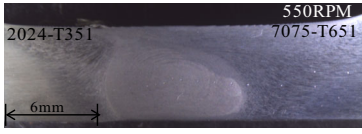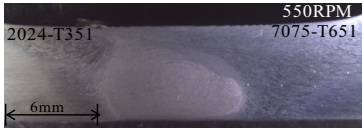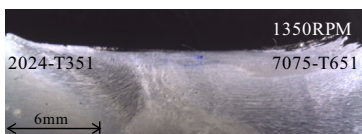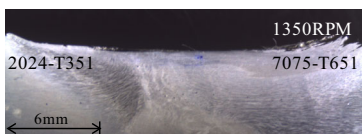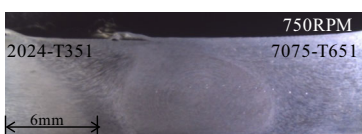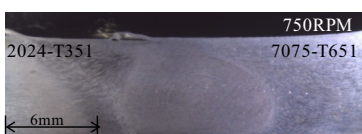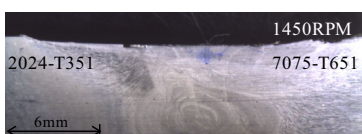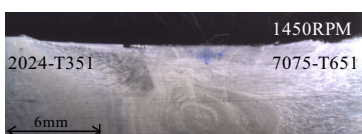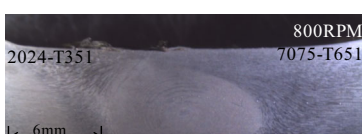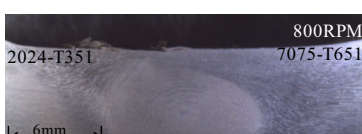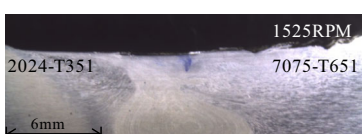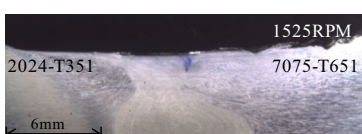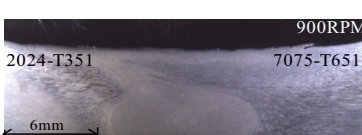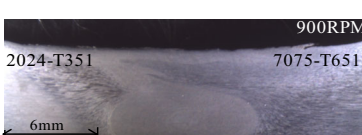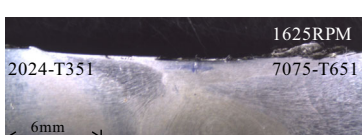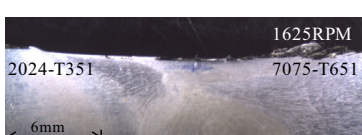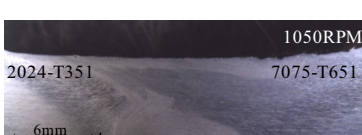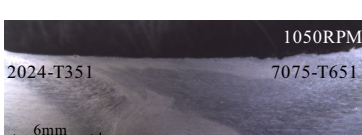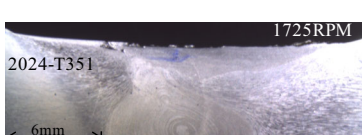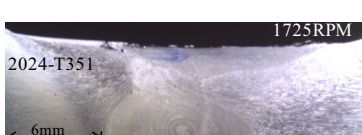
Fig. 16 Low-magnification SEM images for VPD experiment. Plunge depth in 'mm' is highlighted at the top right corner of each figure

severe plastic flow of the material. As the tool traverse speed increases, as presented in Table 5, the width of the WN, TMAZ and HAZ decreased due to the low heat input and less plastic flow, confirming the results reported in the literature (Ref 28, 29, 31, 32). It is evident from the tensile test results (Fig. 13) also that the UTS of these weld joints

Table 4   Optical macrographs for varying tool rotation speeds, optimized plunge depth, 6.2 mm, constant traverse speed, 120 mm/min. Unit of tool rotation speed in 'rpm' mentioned at the top right corner of each figure

	Macrograph			Macrograph	
Tool rotation speed	Advancing side (AS)	Retreating side (RS)	Tool rotation speed	Advancing side (AS)	Retreating side (RS)
450			1250		
550			1350		
750			1450		
800			1525		
900			1625		
1050			1725		

was greatly influenced by these heat inputs and width of WN. The lower UTS observed for a traverse speed range between 20 and 55 mm/min as a result increased width of the softened area than that for higher traverse speed. Classical formation of 'onion rings' was observed in the traverse speed range 55-150 mm/min. However, these 'onion rings' were not identical in shape and these depend on traverse speed. The macrograph images for the traverse speed 137, 160 and 175 mm/min consists of slightly broken WN associated with the less sharp boundary interface between WN and TMAZ of both AS and RS. These sharp boundaries are the result of low heat input and linear microstructure at the interface of the WN/ TMAZ (Ref 33). The presence of these sharp boundaries lead to weakened joints, resulting in lower UTS and YS (see Fig. 13). Therefore, the interface of the WN/TMAZ may be the weakest zone and to be taken into consideration for investigation of the UTS of the FSW dissimilar joints.

Dinaharan et al. (Ref 18), Palanivel et al. (Ref 25) and Amancio-Filho et al. (Ref 26) reported the importance of the mixed flow region in the FSW joints of dissimilar materials to produce a sound weld joints. In general, the WN consists of unmixed region (UMR), mechanically mixed region (MMR) and mixed flow region. Mixed flow is required for the dissimilar materials in order to produce sound welds without any defects. In the present study, the low-magnification SEM images (Fig. 18a and b) at WN exhibiting proper mixed flow consisting of alternate layer-by-layer forming of a lamellae pattern of both AA2024-T351 and AA7075-T651 were also observed from selected varying traverse speed condition. The SEM and back-scattered emission (BSE) images of the transverse section of the FSW joint of the final optimized sample at traverse speed of 150 mm/min with optimum rotation speed, 650 rpm, and optimum plunge depth, 6.2 mm, are shown in Fig. 19(a) and (b).
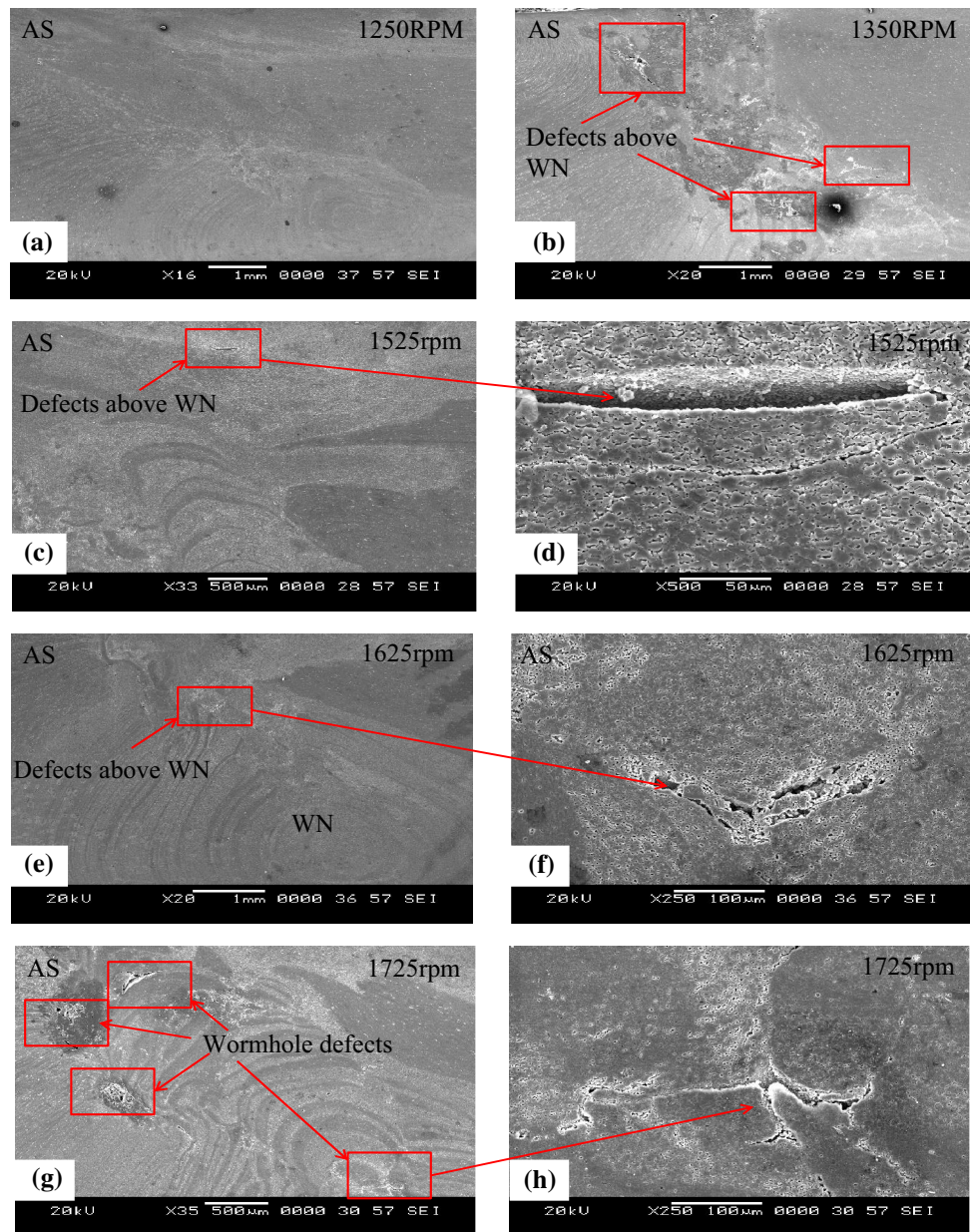
Fig. 17 Low-magnification SEM images of VRS experiment. Unit of rotation speed in 'rpm' mentioned at the top right corner of each figure
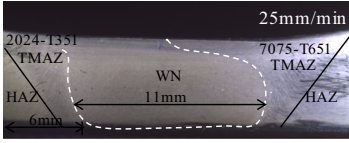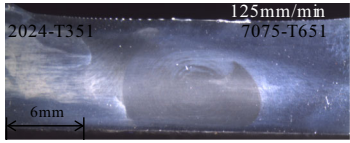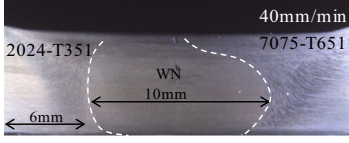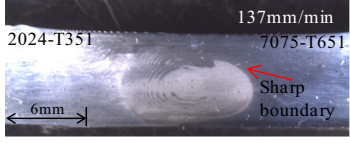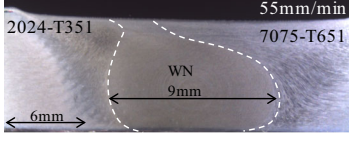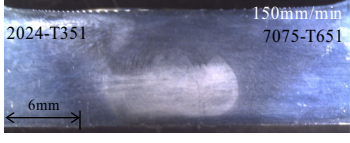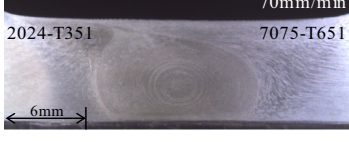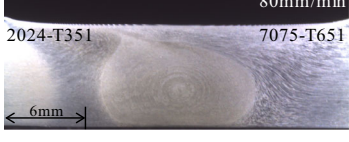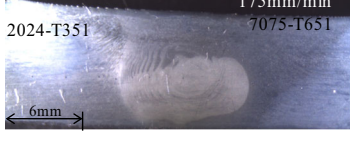
It can be seen from the SEM (Fig. 19a) and BSE (Fig. 19b) images at WN composed of proper mixed flow evidenced by alternate dark and bright lamella pattern as a result of intense plastic deformation caused by stirring action of the tapered threaded tool pin and material flow between the two alloys AA2024-T351/AA7075-T651. The SEM–BSE image as shown in Fig. 19(b) indicates that the dark lamellae in the image results from 2024-T351 and bright lamellae from the 7075-T651 alloy. Figure 19(c) shows SEM images at WN region within the lamellae pattern consisting of very fine equiaxed grains with an average size of 3 to 5 μm.

3.3 Microhardness

The influence of the tool rotation speed on the change in mechanical properties of the dissimilar FSW joints for the condition of VRS is shown using Vicker's microhardness profiles in Fig. 20 and 21. For the VRS range 400-1100 rpm trail, the microhardness profile (see Fig. 20) shows higher hardness at the 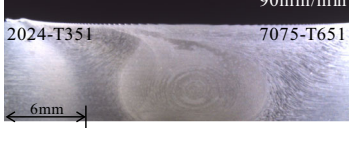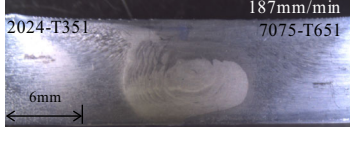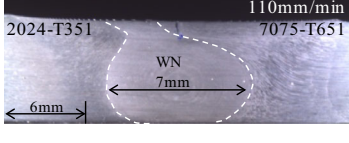WN compared to the base material 2024-T351 hardness, 138Hv. This increase in the hardness at WN may be due to two reasons (i) the formation of 'onion rings' structure at WN consisting of alternate lamellae band pattern having a chemical composition of both AA7075-T651 (high hardness) and AA2024-T351 (low hardness) and (ii) finer grain size at WN compared to the base material. According to the Hall–Petch relation, smaller grain size leads to harder material property. The lower hardness observed in the TMAZ and HAZ of both AS and RS of the joint are the results of severe coarsening and the dissolution of strengthening precipitates (Ref 15, 34-36). It can be observed that VRS range between 400 and 1100 rpm with a constant traverse speed, 120 mm/min, exerted not much considerable difference in average micro-

Table 5   Optical macrographs for varying traverse speeds, optimized plunge depth, 6.2 mm, optimized rotation speed, 650 rpm. Unit of traverse speed in 'mm/min' mentioned at the top right corner of each figure

Tool traverse speed	Macrograph		Tool traverse speed	Macrograph	
	Advancing side (AS)	Retreating side (RS)		Advancing side (AS)	Retreating side (RS)
25			125		
40			137		
55			150		
70			160		
80			175		
90			187		
110			200		
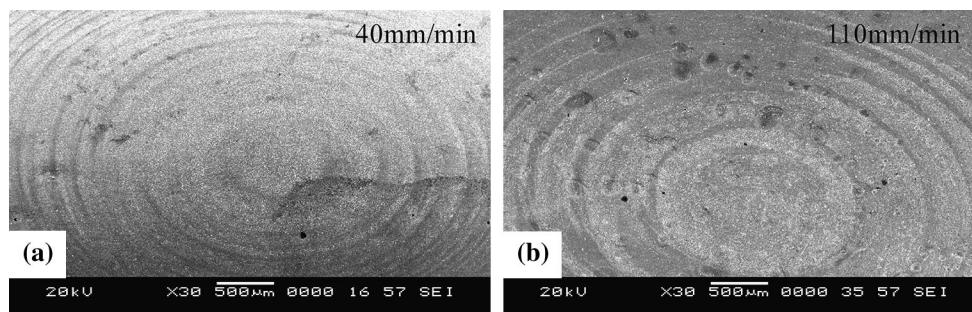
Fig. 18   Low-magnification SEM images of FSW specimens for VTS at (a) 40 mm/min and (b) 110 mm/min. Unit of traverse speed in 'mm/min' highlighted at the top right corner of each figure
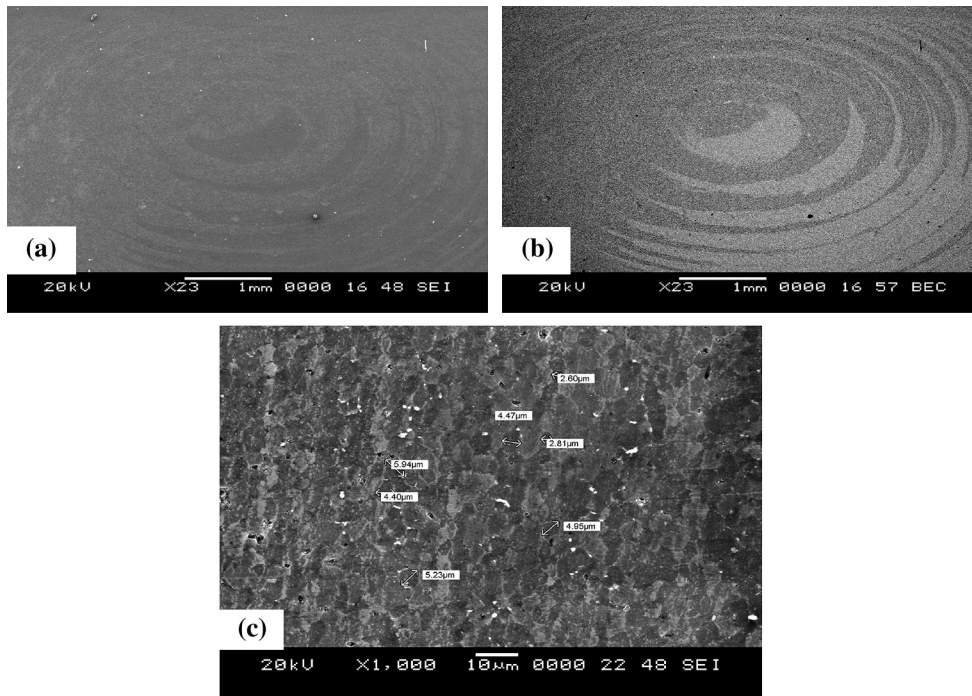
Fig. 19 (a) SEM and (b) SEM–BSE of WN region for the optimized parameters, (c) SEM image for magnification 1000x showing grain size at WN region
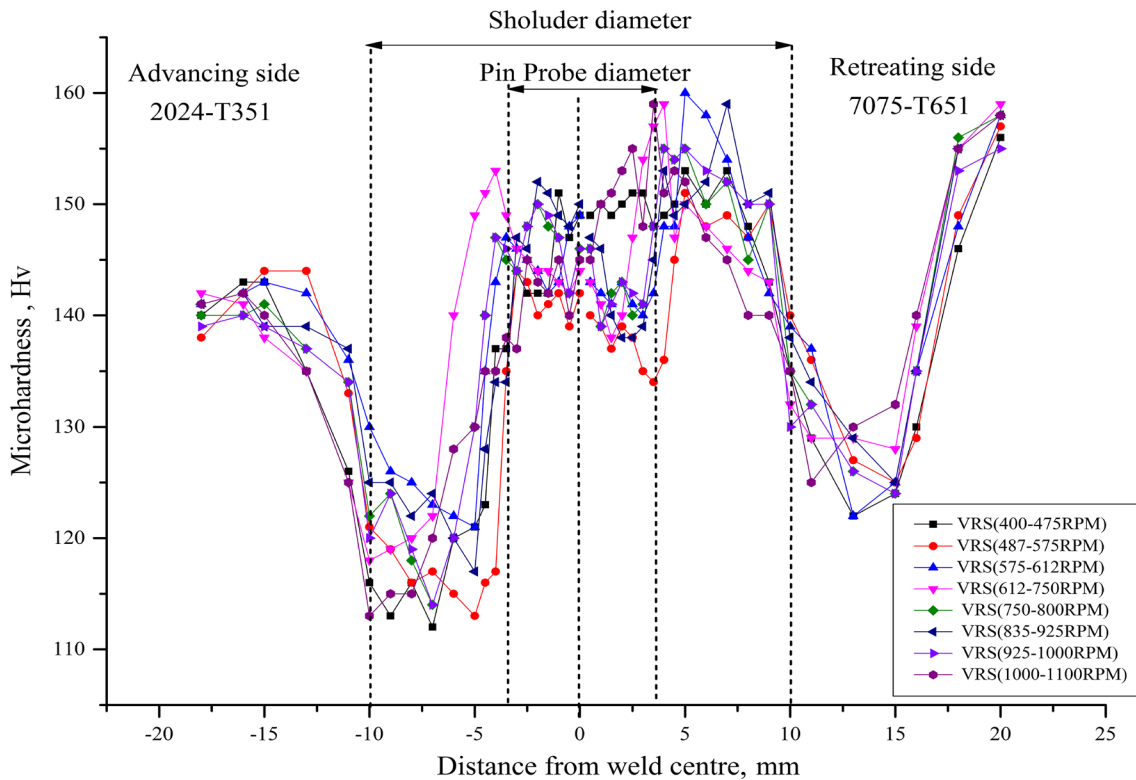
Fig. 20 Hardness profile at mid-thickness transverse to the welding direction of the joints for VRS experiment from 400-1100 rpm

hardness at TMAZ and HAZ of both AS and RS of the joint. However, the hardness at WN slightly increased with an increase in the VRS above 750 rpm. Hardness profile resembles a typical characteristics curve 'W' of a FSW joint.

Microhardness profile for the VRS range between 1100 and 1800 rpm is as shown in Fig. 21. For the rotation speed range between 1275 and 1350 rpm, one can observe a sharp decrease in hardness, viz. 55Hv within the WN owing to the presence of
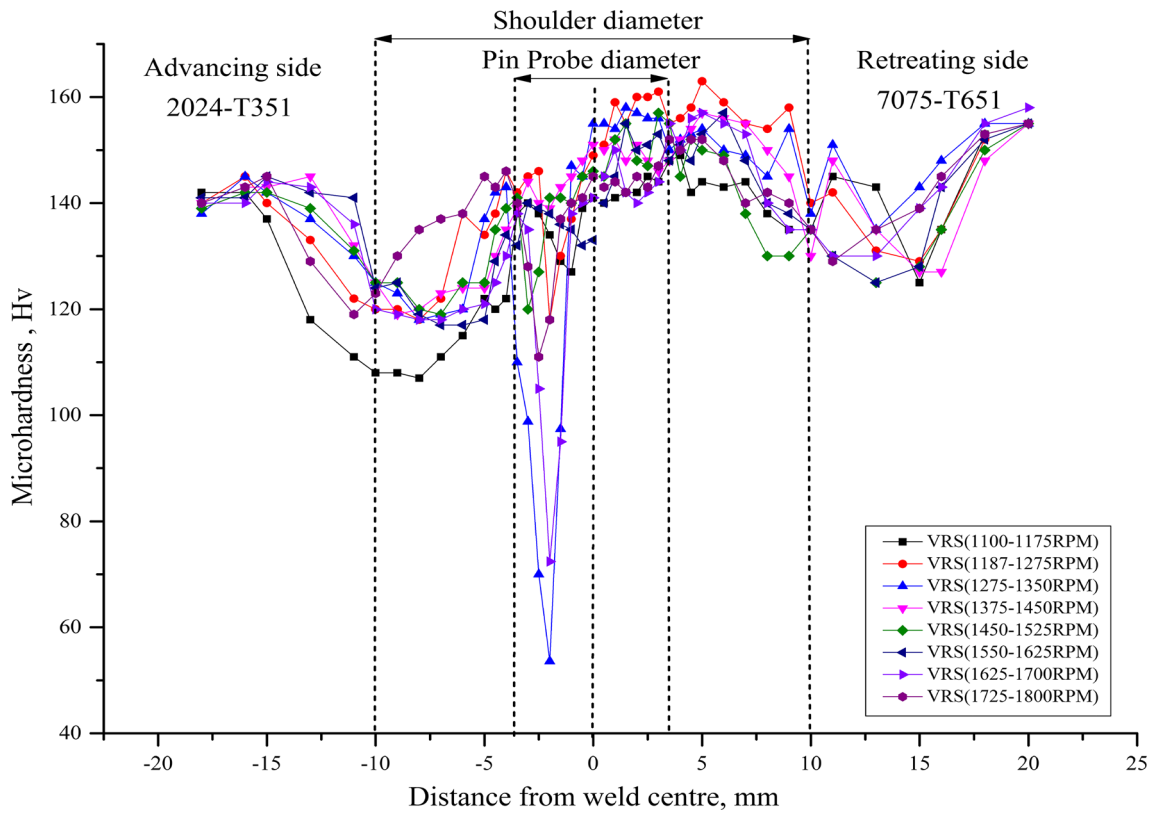
Fig. 21 Hardness profile at mid-thickness transverse to the welding direction of the joints for VRS range 1100-1800 rpm

Fig. 22 Hardness profile at mid-thickness transverse to the welding direction of the joints for VTS ranging between 20 and 120 mm/min

Fig. 23 Hardness profile at mid-thickness transverse to the welding direction of the joints for VTS ranging between 120 and 200 mm/min
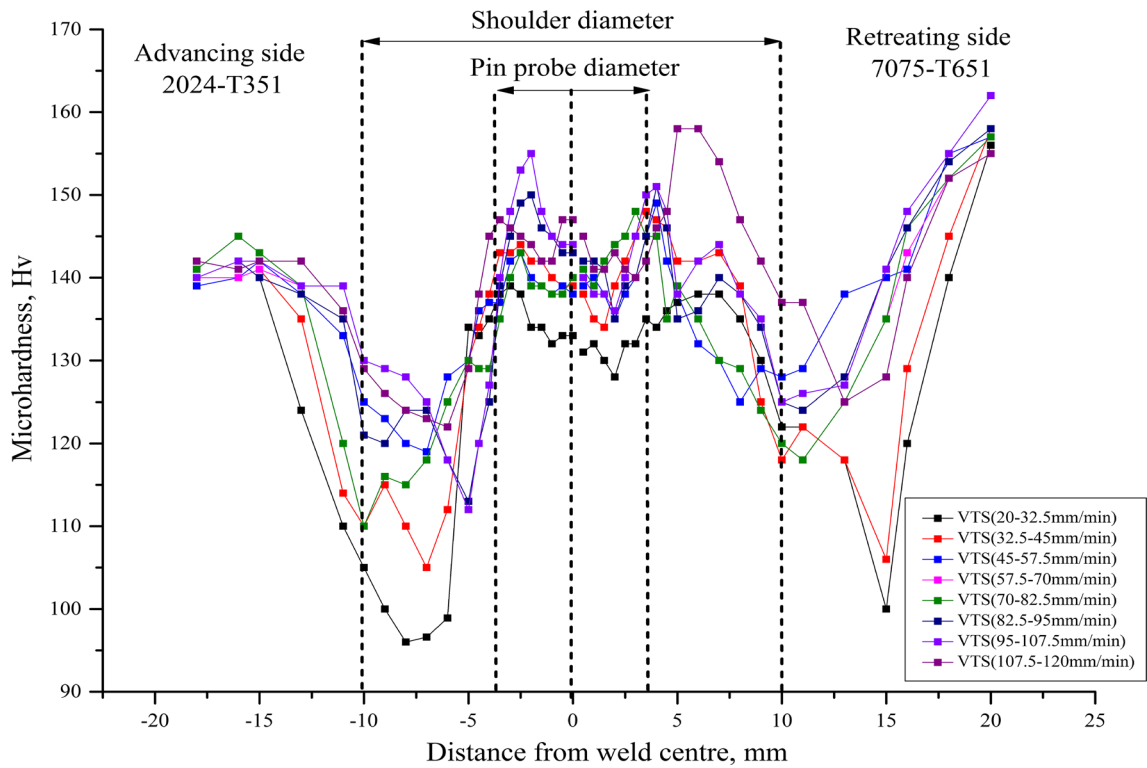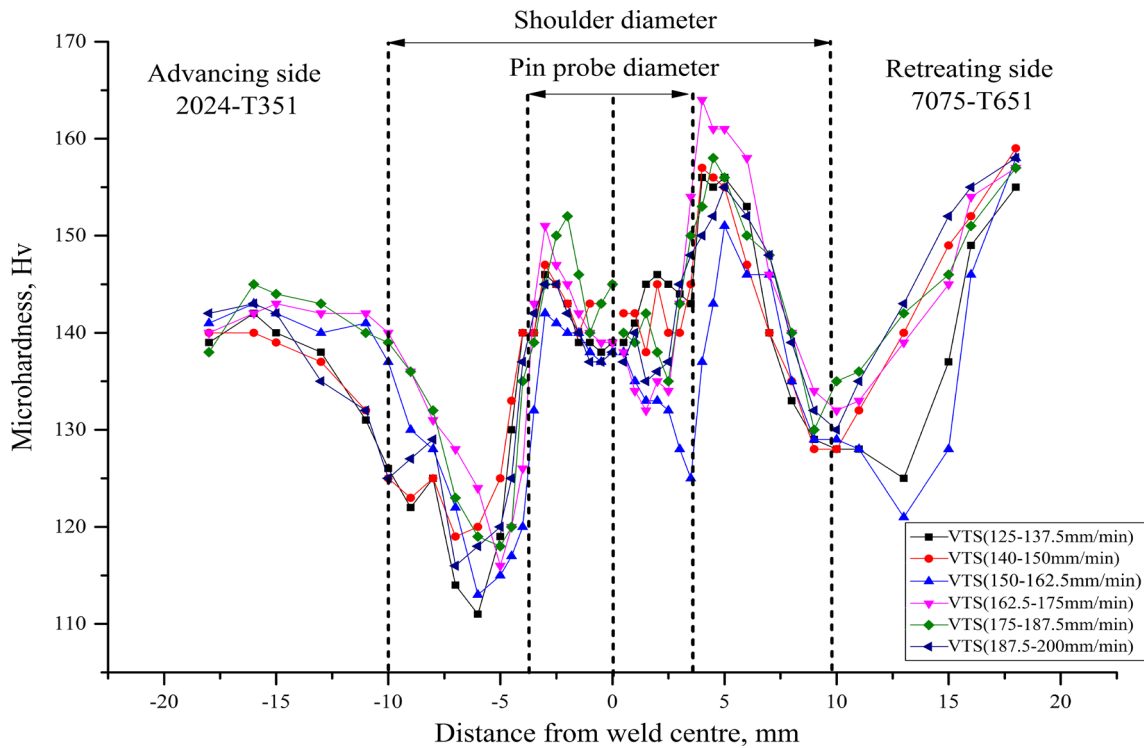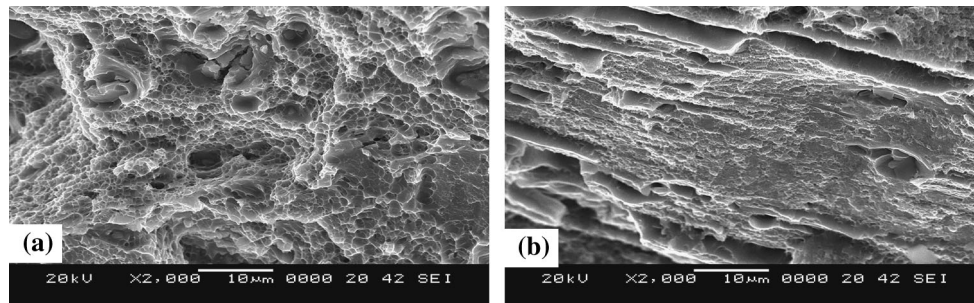

Fig. 24 SEM images of typical fracture surface of base materials; (a) 2024-T351 and (b) 7075-T651

a large number of wormhole defects (Fig. 17b). Higher rotational speed of above 1400 rpm resulted in the higher heat generation and slower cooling rate. Higher heat generation leads to the formation of coarse grains. This led to the formation microvoids and defects (see Fig. 17c-h) and thus result in lower hardness in the AS above the WN compared to the RS. In general, the presence of wormhole defects, coarsening of the grains and lower hardness were observed in the VRS range of 1100-1800 rpm and deteriorated the UTS (Fig. 10) of the FSW joints.

Figure 22 shows the effect of VTS within the range of 20-120 mm/min on the mechanical properties of the dissimilar FSW joint. At the lower traverse speed range of 20 to 50 mm/min, higher temperature and slower cooling rate resulted in a wider softened area (see Table 5) evidenced with a minimum hardness in WN, TMAZ and HAZ regions of both AS and RS. The severe softening behavior at TMAZ and HAZ with a minimum hardness ranging from 95 to 100 Hv was observed at a lower traverse speed range of 20-50 mm/min. For the traverse

speed range from 50 to 120 mm/min, the hardness profile in WN, TMAZ and HAZ shows gradual improvement in the hardness. The tensile properties of the FSW joint have shown (Fig. 13) lower UTS and YS at the traverse speed range of 20-50 mm/min compared to FSW joint produced for the traverse speed range of 80-120 mm/min.

Figure 23 shows that at higher traverse speed range 120-200 mm/min, the softened area becomes narrower because of decreased heat input and faster cooling rate (Ref 28). It was further observed that the softened zone existing near to the shoulder diameter region on both AS and RS (Fig. 22) is shifted near to the pin diameter region (Fig. 23) as the traverse speed increased.

In general, the average microhardness at the WN region for the entire specimen tested for VRS and VTS was found to be higher than that of microhardness measured in TMAZ/HAZ. A minimum hardness was observed in the AS of TMAZ and HAZ region of 2024-T351 alloy in comparison with RS of the AA7075-T651 alloy.
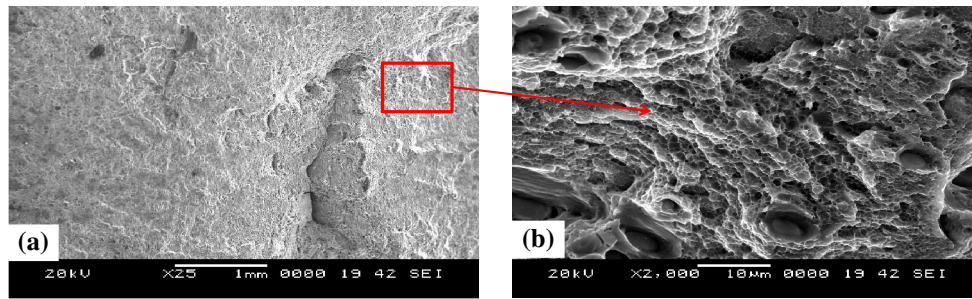
Fig. 25 SEM images of typical fracture surface of FSW specimen for the optimum plunge depth, 6.2 mm, tool rotation speed, 650 rpm, and traverse speed, 150 mm/min
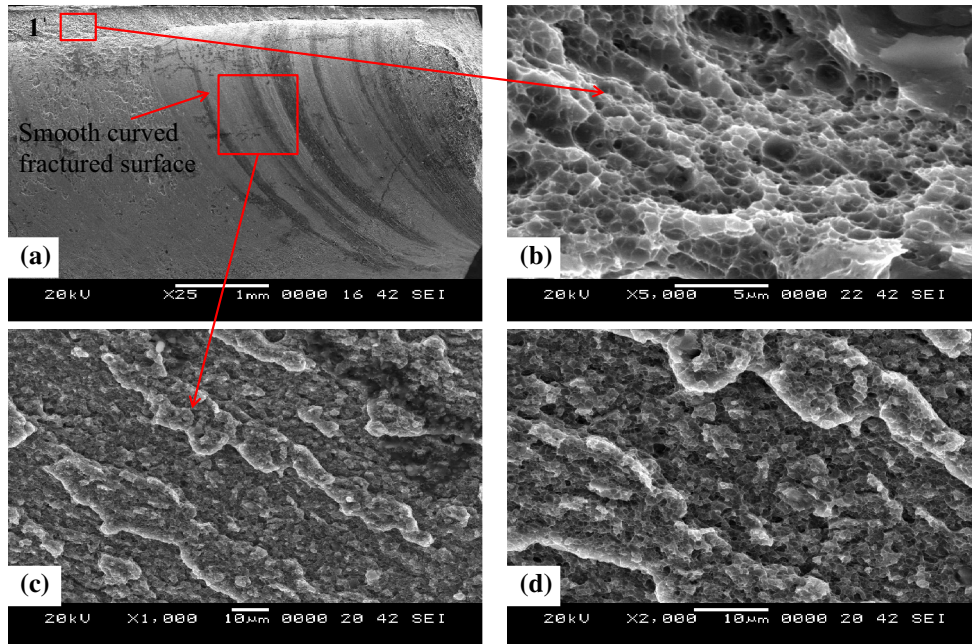
Fig. 26 SEM images of typical fracture surface of FSW specimen for process conditions; plunge depth, 6.2 mm, tool rotation speed, 650 rpm, and traverse speed, 130 mm/min. (a) Fractured surface locations showing alternate stripes, (b) magnified image of the top portion (marked as 1′), (c) magnified portion of square box showing large number of dimples without any microvoids and (d) further magnified image of (c)

3.4 Fractography

The SEM images of the fracture surface of base material 2024-T351 (Fig. 24a) are characterized by a large number of equiaxed very fine dimples of different sizes close to the microscopic voids. The fractography of the tensile specimen of base material 7075-T651 (Fig. 24b) was composed of tearing edges and cleavages. The SEM images shown in Fig. 25 were obtained from the fracture surface of the FSW joint tensile specimen for the optimum process conditions of plunge depth, 6.2 mm, tool rotation speed, 650 rpm, and traverse speed, 150 mm/min. Figure 26 depicts the SEM images obtained from the fracture surface of the FSW joint tensile specimen by keeping both the plunge depth and tool rotation speed as 6.2 mm and 650 rpm, respectively, but traverse speed as 130 mm/min. Fractographic analysis was performed for these two FSW conditions to investigate the failure of the specimen due to lack of metallurgical bonding between two base materials. Further, the fractured surface of the specimen for a
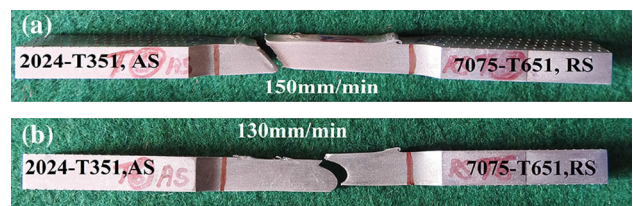
Fig. 27 Fractured specimens; (a) specimen with optimum FSW conditions fractured at HAZ of AS; (b) specimen failed due to lack of bonding at the interface between WN and TMAZ

traverse speed of 130 mm/min is compared with the fractured surface of the specimen obtained under optimum FSW process condition having highest tensile strength. The analysis of the fractured surface (Fig. 25b) from the optimized sample consists of microvoids and a very large number of equiaxed dimples of

different size and shape close to microvoids. The observation of fracture surface indicates that the joint failure is ductile in nature and material showed ductile behavior during fracture progress. This specimen has fractured location in the HAZ of AS (Fig. 27a) and exhibits the fracture surface morphology, which resembles that of base material 2024-T351 (Fig. 24a).

The fractographic analysis of the tensile-tested specimen (Fig. 27b) for the FSW process conditions of plunge depth, 6.2 mm, tool rotation speed, 650 rpm, and traverse speed, 130 mm/min, consists of smooth curved fracture surface features (Fig. 26a) without any severe deformation with an alternate distribution of dark and white stripes. The morphology between these two alternate dark and white stripes is shown in Fig. 26(c). Few specimens have failed due to sharp boundary, or lack of metallurgical bonding between materials shows this kind of fracture surface morphology along the discontinuity region resulting in early failure of the joints. High magnification SEM images (Fig. 26d) at this location show the presence of a large number of small-size dimples and confirm that this specimen too has characteristics of ductile fracture. The fractography analysis carried out at the top portion (shown as '1') of this specimen consists of microvoids surrounded by a large number of dimples (Fig. 26b). Finally, the presence of microvoids and dimples in the entire tensile-tested specimen confirms that the failure characteristics are similar to that of ductile fracture.

4. Conclusions

A bottom-up optimization approach has been used to investigate the influence of friction stir welding parameters such as plunge depth, rotation speed and traverse speed in welded dissimilar aluminum alloys of typical 2024-T351 and 7075-T651. All specimens used in the experiments are plates 6.35 mm thick. Mechanical properties have been evaluated by means of tensile and Vickers microhardness tests. Joints of dissimilar aluminum alloys are obtained for varying plunge depth ranging between 5.8 and 6.2 mm, varying traverse speed ranging 20-200 mm/min and varying rotation speed ranging between 400 and 1800 mm/min. The macro- and microstructure analyses have been carried out for the quality of the joints by optical microscopy and SEM. Further, fractography analysis was carried out for specimen with the optimum FSW parameters.

The important conclusions from this study are as follows

1. The joints fabricated with optimum FSW parameters of tool plunge depth, 6.2 mm, tool rotation speed, 650 rpm, and tool traverse speed, 150 mm/min, resulted in higher UTS of 435 MPa, YS of 290 MPa with a weld joint efficiency of 92% and elongation of 13%. The specimen produced by optimum parameters yielded with defects-free joints. The microstructure of specimen with optimum conditions in the WN region revealed alternate lamellae material flow pattern with better metallurgical properties, defects free and very fine equiaxed grain size of about 3-5 μm.

2. Dissimilar joints of AA2024-T351 and AA7075-T651 showed typical microstructural features of FSW joints consisting of WN, TMAZ and HAZ. Specimens produced for the FSW parameters other than optimum con-

dition show the presence of wormhole defects in WN region and sharp boundary between the interface of WN and TMAZ of both AS and RS. The presence of sharp boundaries proved to be one of the reasons for the decrease in mechanical properties and early failure of the joints by fracture.

3. UTS of the dissimilar FSW joint increased from 173 to 398 MPa for the tool plunge depth ranging between 5.8 and 6.2 mm and keeping both traverse and rotational speeds 120 mm/min and 1000 rpm, respectively, as constant. The YS shows increased trend from 136 to 190 MPa for a tool plunge depth ranging between 5.8 and 6.2 mm. As the tool rotation speed varied from 400 to 650 rpm keeping optimum plunge depth 6.2 mm and constant traverse speed of 120 mm/min, both the UTS and YS increased from 309 to 419 and from 160 to 200 MPa, respectively. Further, for the tool traverse speed ranging between 20 and 150 mm/min with optimum plunge depth of 6.2 mm and rotation speed of 650 rpm, the UTS and YS increased from 290 to 435 and from 170 to 290 MPa, respectively. However, UTS reduces from 435 to 367 MPa with further increase in traverse speed above 150 mm/min.

4. The minimum microhardness of 55Hv is observed for higher rotation speed ranging 1250-1350 rpm at constant traverse speed of 120 mm/min and optimum plunge depth of 6.2 mm. Not much considerable difference in the average values of microhardness is observed for joints produced for lower rotation speeds of 400-1000 rpm at constant traverse speed of 120 mm/min. The microhardness of 95 Hv is observed in the lower traverse speed range between 20 and 50 mm/min at an optimum plunge depth of 6.2 mm and rotation speed of 650 rpm. At higher traverse speed, a shift in the softened zone in the shoulder diameter region to pin probe region was observed. In spite of the different applied FSW parameter conditions, minimum hardness is observed in HAZ on the AA2024-T351 side.

5. Specimen with optimum FSW parameters consists of fracture location at HAZ of the AS of the joint. Fractured surface of all the specimens tested under tensile load showed ductility mechanism of failure characterized with a large number of equiaxed dimples surrounding the microvoids. Some of the specimens that failed due to the presence of sharp boundary had fracture location at the interface of WN/TMAZ of either AS or RS of the joints.

References

1. W.M. Thomas, E.D. Nicholas, J.C. Needam, M.G. Murch, P. Templesmith, and C.J. Dawes, GB Patent Application No. 9125978.8, December 1991 and US Patent No. 5460317, October 1995
2. R.S. Mishra and Z.Y. Ma, Friction Stir Welding and Processing, *Mater. Sci. Eng. Proc. Conf. Reports*, 2005, **50**, 1–78

3. R.S. Mishra, Z.Y. Ma, and I. Charit, Friction Stir Processing: A Novel Technique for Fabrication of Surface Composite, *Mater. Sci. Eng. A*, 2003, **341**(1), p 307–310

4. M.H. Shojaeefard, M. Akbari, A. Khalkhali, P. Asadi, and A.H. Parivar, Optimization of Microstructural and Mechanical Properties of Friction Stir Welding Using the Cellular Automaton and Taguchi Method, *Mater. Des.*, 2014, **64**, p 660–666

5. H. Okuyucu, A. Kurt, and E. Arcaklioglu, Artificial Neural Network Application to the Friction Stir Welding of Aluminum Plates, *Mater. Des.*, 2007, **28**(1), p 78–84

6. M.H. Shojaeefard, R.A. Behnagh, M. Akbari, M.K.B. Givi, and F. Farhani, Modelling and Pareto Optimization of Mechanical Properties of Friction Stir Welded AA7075/AA5083 Butt Joints Using Neural Network and Particle Swarm Algorithm, *Mater. Des.*, 2013, **44**, p 190–198

7. M. Salehi, M. Saadatmand, and J.A. Mohandesi, Optimization of Process Parameters for Producing AA6061/SiC Nanocomposites by Friction Stir Processing, *Trans. Nonferrous Met. Soc. China*, 2012, **22**(5), p 1055–1063

8. Y. Javadi, S. Sadeghi, and M.A. Najafabadi, Taguchi Optimization and Ultrasonic Measurement of Residual Stresses in the Friction Stir Welding, *Mater. Des.*, 2014, **55**, p 27–34

9. S. Rajakumar and V. Balasubramanian, Multi-Response Optimization of Friction-Stir-Welded AA1100 Aluminum Alloy Joints, *J. Mater. Eng. Perform.*, 2012, **21**(6), p 809–822

10. V. Balasubramanian, Relationship Between Base Metal Properties and Friction Stir Welding Process Parameters, *Mater. Sci. Eng. A*, 2008, **480**(1), p 397–403

11. N. Nadammal, S.V. Kailas, and S. Suwas, A Bottom-Up Approach for Optimization of Friction Stir Processing Parameters; A Study on Aluminium 2024-T3 Alloy, *Mater. Des.*, 2015, **65**, p 127–138

12. P. Cavaliere, R. Nobile, F.W. Panella, and A. Squillace, Mechanical and Microstructural Behavior of 2024-7075 Aluminium Alloy Sheets Joined by Friction Stir Welding, *Int. J. Mach. Tools Manuf.*, 2006, **46**(6), p 588–594

13. A.A.M. Da Silva, E. Arruti, G. Janeiro, E. Aldanondo, P. Alvarez, and A. Echeverria, Material Flow and Mechanical Behaviour of Dissimilar AA2024-T3 and AA7075-T6 Aluminium Alloys Friction Stir Welds, *Mater. Des*, 2011, **32**(4), p 2021–2027

14. S.A. Khodir and T. Shibayanagi, Friction Stir Welding of Dissimilar AA2024 and AA7075 Aluminum Alloys, *Mater. Sci. Eng. B*, 2008, **148**(1), p 82–87

15. J.F. Guo, H.C. Chen, C.N. Sun, G. Bi, Z. Sun, and J. Wei, Friction Stir Welding of Dissimilar Materials beTween AA6061 and AA7075 Al Alloys Effects of Process Parameters, *Mater. Des.*, 2014, **56**, p 185–192

16. S.K. Park, S.T. Hong, J.H. Park, K.Y. Park, Y.J. Kwon, and H.J. Son, Effect of Material Locations on Properties of Friction Stir Welding Joints of Dissimilar Aluminium Alloys, *Sci. Technol. Weld. Joining*, 2010, **15**(4), p 331–336

17. R.I. Rodriguez, J.B. Jordon, P.G. Allison, T. Rushing, and L. Garcia, Microstructure and Mechanical Properties of Dissimilar Friction Stir Welding of 6061-to-7050 Aluminum alloys, *Mater. Des.*, 2015, **83**, p 60–65

18. I. Dinaharan, K. Kalaiselvan, S.J. Vijay, and P. Raja, Effect of Material Location and Tool Rotational Speed on Microstructure and Tensile Strength of Dissimilar Friction Stir Welded Aluminum Alloys, *Arch. Civil Mech. Eng.*, 2012, **12**(4), p 446–454

19. J.H. Ouyang and R. Kovacevic, Material Flow and Microstructure in the Friction Stir Butt Welds of the Same and Dissimilar Aluminum Alloys, *J. Mater. Eng. Perform.*, 2002, **11**(1), p 51–63

20. K. Kumar and S.V. Kailas, The Role of Friction Stir Welding Tool on Material Flow and Weld Formation, *Mater. Sci. Eng., A*, 2008, **485**(1), p 367–374

21. N.S. Sundaram and N. Murugan, Tensile Behavior of Dissimilar Friction Stir Welded Joints of Aluminium Alloys, *Mater. Des.*, 2010, **31**(9), p 4184–4193

22. G. Buffa, J. Hua, R. Shivpuri, and L. Fratini, Design of the Friction Stir Welding Tool Using the Continuum Based FEM Model, *Mater. Sci. Eng. A*, 2006, **419**(1), p 381–388

23. P. Vijayavel, V. Balasubramanian, and S. Sundaram, Effect of Shoulder Diameter to Pin Diameter (D/d) Ratio on Tensile Strength and Ductility of Friction Stir Processed LM25AA-5% SiCp Metal Matrix Composites, *Mater. Des.*, 2014, **57**, p 1–9

24. S. Rajakumar, C. Muralidharan, and V. Balasubramanian, Influence of Friction Stir Welding Process and Tool Parameters on Strength Properties of AA7075-T 6 Aluminium Alloy Joints, *Mater. Des.*, 2011, **32**(2), p 535–549

25. R. Palanivel, P.K. Mathews, N. Murugan, and I. Dinaharan, Effect of Tool Rotational Speed and Pin Profile on Microstructure and Tensile Strength of Dissimilar Friction Stir Welded AA5083-H111 and AA6351-T6 Aluminum Alloys, *Mater. Des.*, 2012, **40**, p 7–16

26. S.T. Amancio-Filho, S. Sheikhi, J.F. dos Santos, and C. Bolfarini, Preliminary Study on the Microstructure and Mechanical Properties of Dissimilar Friction Stir Welds in Aircraft Aluminium Alloys 2024-T351 and 6056-T4, *J. Mater. Process. Technol.*, 2008, **206**(1), p 132–142

27. A. Steuwer, M.J. Peel, and P.J. Withers, Dissimilar Friction Stir Welds in AA5083-AA6082: The Effect of Process Parameters on Residual Stress, *Mater. Sci. Eng. A*, 2006, **441**(1), p 187–196

28. M. Peel, A. Steuwer, M. Preuss, and P.J. Withers, Microstructure, Mechanical Properties and Residual Stresses as a Function of Welding Speed in Aluminium AA5083 Friction Stir Welds, *Acta Mater.*, 2003, **51**(16), p 4791–4801

29. F. Zhang, X. Su, Z. Chen, and Z. Nie, Effect of Welding Parameters on Microstructure and Mechanical Properties of Friction Stir Welded Joints of a Super High Strength Al-Zn-Mg-Cu Aluminum Alloy, *Mater. Des.*, 2015, **67**, p 483–491

30. D. Trimble, G.E. O'Donnell, and J. Monaghan. Characterization of Tool Shape and Rotational Speed for Increased Speed During Friction Stir Welding of AA2024-T3, *J. Manuf. Process*, 2015, **17**, p 141–150

31. S. Lomolino, R. Tovo, and J. dos Santos, On the Fatigue Behaviour and Design Curves of Friction Stir Butt-Welded Al Alloys, *Int. J. Fatigue*, 2005, **27**(3), p 305–316

32. D. Li, X. Yang, L. Cui, F. He, and H. Shen, Effect of Welding Parameters on Microstructure and Mechanical Properties of AA6061-T6 Butt Welded Joints by Stationary Shoulder Friction Stir Welding, *Mater. Des.*, 2014, **64**, p 251–260

33. Z. Zhang, B.L. Xiao, and Z.Y. Ma, Hardness Recovery Mechanism in the Heat-Affected Zone During Long-Term Natural Aging and Its Influence on The Mechanical Properties and Fracture Behavior of Friction Stir Welded 2024Al-T351 Joints, *Acta Mater.*, 2014, **73**, p 227–239

34. G. D'Urso, C. Giardini, S. Lorenzi, and T. Pastore, Fatigue crack Growth in the Welding Nugget of FSW Joints of a 6060 Aluminum Alloy, *J. Mater. Process. Technol.*, 2014, **214**(10), p 2075–2084

35. Y.S. Sato, H. Kokawa, M. Enomoto, and S. Jogan, Microstructural Evolution of 6063 Aluminum During Friction-Stir Welding, *Metall. Mater. Trans. A*, 1999, **30**(9), p 2429–2437

36. J.Q. Su, T.W. Nelson, R. Mishra, and M. Mahoney, Microstructural Investigation of Friction Stir Welded 7050-T651 Aluminium, *Acta Mater.*, 2003, **51**(3), p 713–729

37. Y.G. Kim, H. Fujii, T. Tsumura, T. Komazaki, and K. Nakata, Three Defect Types in Friction Stir Welding of Aluminum Die Casting Alloy, *Mater. Sci. Eng., A*, 2006, **415**(1), p 250–254